International Journal of Mechanical Sciences 319 (2026) 111539

Contents lists available at ScienceDirect

International Journal of Mechanical Sciences

journal homepage: www.elsevier.com/locate/ijmecsci

Nonlinear oscillations of floating offshore wind turbines under wave excitation ☆

Marco Luciani, Stefano Lenci *

Department of Civil and Building Engineering, and Architecture (DICEA), Polytechnic University of Marche (UNIVPM), Via Brecce Bianche, Ancona, 60131, Italy

ARTICLE INFO

Keywords:
Nonlinear dynamics
Floating offshore wind turbines (FOWTs)
Parametric resonance
Third vs fifth order solutions
Small vs large amplitude attractors
Competing resonant and non-resonant oscillations

ABSTRACT

An approximate planar two-Degrees-Of-Freedom (DOF) analytical model is developed to investigate the nonlinear dynamic response of a Floating Offshore Wind Turbine (FOWT), mounted on a spar platform, under parametric excitations induced by the periodic variation of the buoyancy force due to sea waves. The equations of motion, studied under the main parametric resonance (PR) condition, account for the linear and nonlinear hydrostatic stiffnesses and their squares as explicit time-dependent functions of the free-surface elevation. The main novelties are: (i) a rigorous derivation of the wave-elevation-dependent linear and nonlinear hydrostatic stiffnesses, retaining the associated higher-harmonic parametric components; (ii) a fifth-order Multiple Time Scales Method (MTSM) analysis of the primary 2:1 parametric resonance, predicting small-amplitude resonant period-2 oscillations emerging from subcritical and supercritical Hopf bifurcations of the rest position; (iii) a complementary Harmonic Balance Method (HBM) study that reveals, beyond standard low-order formulations, a detached and non-resonant family of large-amplitude period-1 solutions; and (iv) a basin-based assessment of practical pitch stability. Numerical continuation, direct time-domain integrations, and basin-of-attraction computations confirm the unexpected coexistence between the classical small-amplitude resonant period-2 response and the detached non-resonant period-1 oscillation at finite and large amplitude. Remarkably, the period-1 attractor can exhibit wide basins of attraction even when the rest state is locally stable and within damping, wave-amplitude, and frequency ranges commonly considered acceptable in design practice, thus turning a seemingly safe operating point into a practically vulnerable one. These results demonstrate that conventional linear (and low-order nonlinear) analyses may systematically underestimate the risk of wave-induced large-amplitude pitch motions in spar-type FOWTs, and they provide a lightweight analytical framework together with basin-based robustness indicators for early-stage design and control screening.

1. Introduction

The increasing global demand for energy, driven by economic development and population growth, has led to a dramatic increase in greenhouse gas emissions, primarily due to the widespread use of fossil fuels. According to the International Energy Agency, fossil fuels still account for over 80% of the world's energy supply, contributing significantly to climate change and environmental degradation [1]. To address this urgent issue, renewable energy sources such as solar, hydro, and wind have emerged as essential components in the transition to a more sustainable energy future [2,3].

Among these, offshore wind energy has gained particular attention due to its high resource potential, especially in deep-water regions where wind conditions are more stable and intense [4]. In this context, FOWTs represent a revolutionary technology that overcomes the limitations of traditional bottom-fixed turbines, which are restricted to shallow waters (typically < 60 m). FOWTs, mounted on floating platforms anchored to the seabed, enable energy harvesting in deeper offshore areas, thus opening access to vast untapped wind resources [5,6]. Although the new frontiers are towards Floating Modular Energy Islands [7,8], much understanding is still missing for FOWTs, in particular for their nonlinear dynamical behavior [9], despite the fact that some FOWTs are already operating [10].

Compared to their fixed-bottom counterparts, FOWTs offer several engineering and strategic advantages, such as wider geographical deployment, higher wind speeds, reduced visual and noise impact, and a modular and scalable design [11,12]. However, despite these promising aspects, FOWTs pose new significant engineering challenges, particularly in terms of structural stability and dynamic response. Due to their

☆ This article is part of a Special issue entitled: 'IUTAM Symposium on green energy generation' published in International Journal of Mechanical Sciences.

* Corresponding author.
E-mail addresses: m.f.luciani@pm.univpm.it (M. Luciani), lenci@univpm.it (S. Lenci).

https://doi.org/10.1016/j.ijmecsci.2026.111539
Received 2 November 2025; Received in revised form 19 March 2026; Accepted 24 March 2026
Available online 2 April 2026
0020-7403/© 2026 The Author(s). Published by Elsevier Ltd. This is an open access article under the CC BY-NC-ND license (http://creativecommons.org/licenses/by-nc-nd/4.0/).

floating nature, these systems are subject to complex coupled aero-hydro-servo-dynamic loads, which include both aerodynamic forces from turbulent wind and hydrodynamic forces from waves, currents, and mooring-line dynamics [13].

Among the various structural challenges affecting FOWTs, PR represents a critical source of dynamic instability [14]. This phenomenon occurs when system parameters, such as stiffness or inertia, vary periodically in time, leading to potentially large oscillations even under small excitations.

The first mathematical description of PR dates back to the classical Mathieu's equation [15], originally introduced in 1868 to describe the vibration of an elliptical membrane. Over the decades, many fundamental contributions have expanded our understanding of PR [16–19]. These foundational works continue to serve as cornerstones in the theoretical understanding of PR and are directly relevant to the analysis of complex engineering systems, where time-varying parameters naturally emerge due to environmental excitations and structural motion.

As regards FOWTs, even though new stability improvement methods have recently been proposed for spar-buoy FOWTs [20], spar platforms demonstrate an outstanding vulnerability to PR phenomena. As a matter of fact, Ma et al. [21] investigated a tethered-buoy system and showed that parametric excitation can induce large-amplitude oscillations and overturning, with good agreement between theory, experiments, and simulations. Choi et al. [22,23] demonstrated, via model tests and numerical analyses, that spar-type floating platforms may experience pitch PR under regular wave excitation. Giorgi et al. [24] showed that PR in the roll and pitch DOF can be caused by nonlinear coupling between different modes of motion. Jingrui et al. [25] demonstrated that the spar platform may exhibit complicated dynamic behaviors when the sum-type combination resonance occurs. Sang et al. [26] investigated how wave-induced variations of the hydrodynamic coefficients can trigger significant nonlinear amplification and instability in the coupled heave-pitch response. Gavassoni et al. [27] analytically investigated the heave–pitch dynamics of a conceptual spar platform through nonlinear vibration modes, revealing parametric resonance phenomena. Rho et al. [28] demonstrated that conventional spar platforms may undergo Mathieu-type pitch instability in regular waves when the pitch natural period approaches twice the heave period. Shen and Tang [29] carried out a stochastic analysis, showing that random waves can trigger Mathieu-type pitch instability and internal heave–pitch resonance through energy transfer from heave to pitch. Koo et al. [30] demonstrated that the interaction with mooring and riser dynamics may induce a pronounced Mathieu-type instability in the pitch motion of spar platforms. Jang and Kim [31] showed through nonlinear time-domain simulations that spar platforms may experience strong heave-to-pitch and heave-to-heave Mathieu instability due to nonlinear hydrostatic and Froude–Krylov forces. Li et al. [32] analyzed the nonlinear pitch response of a spar-type FOWT under parametric excitation, considering the interaction of wind, wave and vortex induced vibrations loading. Aziminia et al. [33] developed an efficient method to determine PR instability region for spar platforms. Ghozlane et al. [34] investigated the nonlinear dynamics of a spar-type FOWT, revealing multiple coexisting periodic solutions and demonstrating how internal resonances and parametric excitation influence pitch instability. Zhao et al. [35] carried out a dedicated numerical and analytical study of the 2:1 parametric pitch resonance of a spar-buoy under regular and irregular sea waves.

Recent years have seen a rapid expansion of FOWT dynamic-response studies, with a strong emphasis on high-fidelity, fully coupled CFD frameworks to resolve nonlinear wave–structure interaction under complex and extreme conditions, like focused wave groups and wave–current environments [36–39]. These approaches are essential to reproduce transient loads and global motions of platforms, but their computational cost limits systematic parametric sweeps and they do not provide a dedicated, lightweight stability layer tailored to the Mathieu-type pitch instability mechanism that is particularly critical for spar-type systems. However, despite the substantial progress on parametric responses of floating bodies, the state of the art for spar-type FOWTs in pitch still exhibits four focused gaps that directly hinder early-stage screening and robustness assessment.

(i) Modeling gap (explicit hydrostatic modulation): reduced-order pitch models typically represent wave-induced parametric excitation via a modulation of the linear hydrostatic term only, while nonlinear terms are kept constant or truncated without an explicit dependence on the instantaneous free-surface elevation. A compact pitch model where both linear and nonlinear hydrostatic stiffnesses are rigorously derived from the buoyancy moment and expressed as explicit time-varying functions of the wave elevation (and its square) for a realistic spar-type FOWT is still missing.

(ii) Analysis gap (high-order and detached solutions): most analytical treatments of FOWT parametric resonance remain within third-order multiple-time-scales approximations and primarily target the main 2:1 tongue. High-order analytical equations for the primary 2:1 parametric pitch resonance of a spar-type FOWT, explicitly accounting for the simultaneous modulation of linear and nonlinear time-varying terms and for the emergence of detached large-amplitude branches, are still not available. In particular, a framework able to predict the coexistence of resonant period-2 solutions and non-resonant detached period-1 pitch responses has not yet been established.

(iii) Robustness gap (basin-based practical stability): beyond local bifurcation thresholds, spar-type FOWTs require a robustness-oriented view. A basin-based assessment of pitch stability under parametric excitation remains largely unexplored, and the extent to which small-amplitude and large-amplitude attractors can dominate phase space and undermine the practical stability of the rest position has not been quantified.

(iv) Design-integration gap (a PR-oriented stability layer): Although coupled aero–hydro–servo–elastic frameworks and optimization pipelines are advancing, they typically lack a parametric-resonance-oriented module that can be embedded as a low-cost screening layer to identify when linear or low-order nonlinear checks may severely underestimate the risk of large pitch motions in spar platforms.

To address gaps (i)–(iv), this paper provides four targeted contributions for spar-type FOWTs in pitch.

(i) It derives a compact 2-DOF mechanical model in which the hydrostatic overturning moment is asymptotically expanded up to third order, yielding explicitly time-varying linear and nonlinear stiffness terms that depend on the free-surface elevation and its square (thereby retaining higher-harmonic parametric components and amplitude-dependent stiffness in closed form).

(ii) Under the main 2:1 parametric-resonance condition, it combines fifth-order Multiple Time Scales and Harmonic Balance analyses, resulting in high-order reduced equations (with effective quintic nonlinearity) that enable a systematic analytical characterization of the local bifurcation scenario, including the birth and stability of both resonant period-2 and detached non-resonant period-1 solutions.

(iii) It validates the coexistence scenario through numerical continuation and long-time direct integrations, and computes the corresponding basins of attraction, providing, within the spar-type FOWT context, a direct basin-based measure of practical pitch stability under parametric excitation.

(iv) It translates these dynamical findings into explicit engineering implications: large-amplitude attractors with sizeable basins can exist within wave-excitation and damping ranges often considered acceptable, showing that purely linear (or low-order) assessments may systematically underestimate the risk of large pitch motions.

The paper is organized as follows. The mechanical model is obtained in Section 2 by considering the various mechanical aspects that contribute to the equations of motion, which are subsequently reported in Section 3. A third order approximation is considered to facilitate the solution. Approximate analytical solutions are reported in the subsequent section, by the Multiple Time Scale Method for the

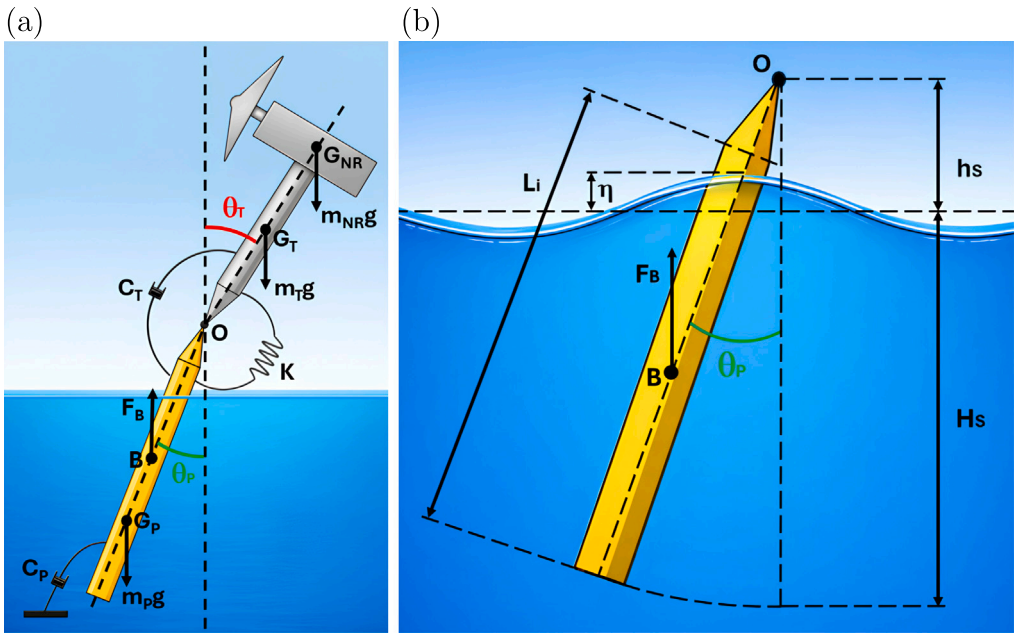

Fig. 1. Schematic representations of (a) the 2-DOF model for the wind turbine tower installed on a floating spar platform, with sea at rest, and (b) the rotational effect provided by the buoyancy force, with sea waves.

period-2 resonant solution (Section 4) and by the Harmonic Balance method for the period-1 non resonant solution (Section 5). By choosing the values of the parameters corresponding to a realistic system, the main results are illustrated in Section 6 with the help of bifurcation diagrams, time histories, and basins of attraction. The paper ends with some conclusions and suggestions for further development (Section 7).

2. The mechanical system

This section summarizes the assumptions used to model the considered FOWT, aiming at a formulation as simple as possible while retaining the key dynamical features of interest. The system in Fig. 1(a) follows the assumptions in [40] and represents a wind turbine installed on a floating spar platform.

Since the fore–aft direction experiences the highest wind- and wave-induced loading and thus the largest tower fatigue damage [41], the tower dynamics is restricted to the fore–aft plane. Moreover, platform pitch has been shown to drive the largest tower bending for both barge and spar concepts [42], and pitch oscillations are markedly amplified in spars under parametric resonance [43]. Accordingly, only two DOF are retained: the tower fore–aft bending angle ϑ_T and the platform pitch angle ϑ_P. The tower is modeled as a rigid inverted pendulum rotating about the hinge O, connected to the spar top through a rotary spring K and a rotary damper C_T; K includes a linear and a cubic component (K_1, K_3). The points G_T and G_{NR} denote the centers of mass of the tower and of the nacelle–rotor assembly, respectively. The spar platform is modeled as a rigid pendulum rotating about O, with a rotary damper C_P at its bottom accounting for sea-induced dissipation; B and G_P are the centers of buoyancy and mass of the spar, respectively.

It must be noted that wind thrust and blade control are intentionally neglected in the present study to isolate the wave–hydrostatic mechanism responsible for parametric resonance in spar-type FOWTs. Abe et al. [44], indeed, demonstrated that the change in the wetted area shifts the center of buoyancy and thus alters the metacentric height, resulting in a time-variable hydrostatic stiffness for pitch and roll motions. This time-varying hydrostatic stiffness is potentially able to trigger PR in pitch and roll DOF. Furthermore, in parked conditions the blades are typically pitched toward feather to minimize aerodynamic loads; this means that wind mainly introduces a mean offset and an additional (often frequency-dependent) aerodynamic damping or forcing contribution. These effects can shift the equilibrium and modify the quantitative boundaries of the parametric-instability regions. Therefore, since the goal of this work is to isolate and characterize the wave-induced hydrostatic stiffness modulation mechanism, the present reduced-order model does not consider aerodynamic loads and focuses on the wave-induced parametric response layer. The extension to fully coupled aero–hydro–servo–mooring dynamics is deferred to future work, where high-fidelity time-domain tools are typically required. For consistency with this objective (i.e., isolating wave-induced PR), two additional simplifications are introduced: (i) a deliberately reduced model is adopted to capture the essential mechanisms with a tractable mathematical structure, suitable for pre-design analyses; and (ii) the heave displacement is neglected, while pitch is retained. More refined multi-DOF and high-fidelity hydrodynamic models are deferred to future work, where analytical developments are typically replaced by computationally intensive simulations [45].

The analytical model has been experimentally validated against published wave-tank measurements of Mathieu-type pitch instability for a spar platform [46].

2.1. The linear and nonlinear stiffnesses of the rotary spring

To compute the stiffnesses K_1 (the linear part) and K_3 (the cubic nonlinear part) of the rotary spring K, we follow the same approach of [47,48]. The wind turbine tower is considered as a cantilevered vertical beam with a horizontal force Q on the top; because of the axial symmetry it is possible to consider a planar problem.

By elaborating the results of [47,48] we obtain

$$M = QH = \frac{EI_a}{H}\left[3(\vartheta_T - \vartheta_P) + \frac{108}{35}(\vartheta_T - \vartheta_P)^3 + \dots\right]. \tag{1}$$

where H is the height of the beam, EI_a the bending stiffness. Therefore,

$$K_1 = \frac{3EI_a}{H}, \quad K_3 = \frac{108EI_a}{35H}. \tag{2}$$

2.2. The effect of the masses in the turbine tower

The contributions, provided by the masses in the wind turbine, are shown in Fig. 1(a).

Let us define the auxiliary term K_{MT} as follows:

$$K_{\mathrm{MT}} = m_T\, g\, \overline{OG_T} + m_{NR}\, g\, \overline{OG_{NR}}, \tag{3}$$

where g is the gravitational acceleration, m_T is the mass of the tower, $\overline{OG_T}$ is the distance between the pole O and the center of mass of the tower, m_{NR} is the mass of the nacelle, the rotor and the blades, $\overline{OG_{NR}}$ is the distance between the pole O and the center of mass of the nacelle and the rotor. So, the "destabilizing" moment around the pole O, due to the weight of the wind tower and blades is given by:

$$M(O)_{\text{ masses turbine}} = -K_{\mathrm{MT}}\, \sin(\vartheta_T) = -K_{\mathrm{MT}}\, \vartheta_T + \frac{1}{6} K_{\mathrm{MT}}\, \vartheta_T^3 + \dots . \tag{4}$$

2.3. The effect of the mass of the spar platform

The spar platform utilizes the "gravity-stabilization" [49] effect. This means that a ballast is located at the bottom of the platform, which, together with the mooring lines (not considered in this work), lowers the center of gravity of the entire platform system (spar + ballast + mooring lines). In this way, the stabilizing moment, due to the weight force, counteracts the overturning effect of the buoyancy force. The contribution, provided by the mass of the floating spar platform, is shown in Fig. 1(a).

Let us define the auxiliary term K_{MP} as follows:

$$K_{\mathrm{MP}} = m_P\, g\, \overline{OG_P}, \tag{5}$$

where g is the gravitational acceleration, m_P is the mass of the whole spar platform system and $\overline{OG_{\mathrm{P}}}$ is the distance between the pole O and the center of mass of the whole spar platform system. So, the "stabilizing" moment around the pole O due to the weight of the spar platform is given by:

$$M(O)_{\text{ masses spar}} = K_{\mathrm{MP}}\, \sin(\vartheta_P) = K_{\mathrm{MP}}\, \vartheta_P - \frac{1}{6} K_{\mathrm{MP}}\, \vartheta_P^3 + \dots . \tag{6}$$

2.4. The effect of the buoyancy force

To compute the effect of the buoyancy force, the same assumptions explained in [50] are used.

The spar platform is geometrically a cylinder with a constant circular cross-section and the diameter of the base area is significantly smaller than the height of the entire cylinder. Therefore, the following approximations are acceptable. As illustrated in Fig. 1(b), the spar platform undergoes rotational motion around the point O and is affected by an incident water wave, whose surface elevation $\eta(t)$ varies periodically over time,

$$\eta(t) = W \cos(\omega t), \tag{7}$$

where W is the wave amplitude, ω is the wave frequency and t represents the time. When the platform is at rest ($\vartheta_P = 0$), the submerged portion of the platform is H_s long, while the portion above the water is h_s. The buoyancy force F_B is applied at the center of buoyancy B, which is at the midpoint of the height of the submerged portion of the platform. For $\theta_P \neq 0$, this submerged portion is considered to have a length L_i, which takes the value

$$L_i = H_s + h_s - \frac{h_s - \eta(t)}{\cos(\vartheta_P)}. \tag{8}$$

Therefore, the buoyancy force is given by

$$F_B = \rho\, g\, A_P\, L_i, \tag{9}$$

where ρ is the density of water and A_p is the base area of the spar platform, and the "overturning" moment $M(O)_B$, due to the buoyancy force, is

$$M(O)_B = -F_B\, \overline{OB}\, \sin\vartheta_P = K_{1\mathrm{B}}\, \vartheta_P + K_{3\mathrm{B}}\, \vartheta_P^3 + \dots , \tag{10}$$

where

$$\overline{OB} = \frac{h_S - \eta(t)}{\cos(\vartheta_P)} + \frac{L_i}{2}, \tag{11}$$

$$K_{1\mathrm{B}} = \rho\, g\, A_P \left(\frac{\eta(t)^2}{2} - \eta(t) h_s - \frac{H_s^2}{2} - H_s h_s \right), \tag{12}$$

$$K_{3\mathrm{B}} = \rho\, g\, A_P \left(\frac{5\eta(t)^2}{12} - \frac{5\eta(t) h_s}{6} + \frac{H_s^2}{12} + \frac{H_s h_s}{6} + \frac{h_s^2}{2} \right). \tag{13}$$

This modeling step introduces key differences with respect to existing analytical spar-FOWT formulations. Previous approaches either adopt linear restoring stiffness and neglect nonlinearities [33,51], or retain cubic terms in ϑ_P, while assuming stiffness coefficients that are constant and independent of wave elevation [34,44]. Here, instead, $K_{1\mathrm{B}}$ and $K_{3\mathrm{B}}$ in (12) and (13) depend explicitly on $\eta(t)$ and $\eta(t)^2$, thereby retaining higher-harmonic parametric components and wave-amplitude-dependent stiffness variations that are central to PR. Moreover, while cubic coefficients in earlier models are often heuristic or derived under static conditions [34,44], $K_{3\mathrm{B}}$ in (13) follows from a rigorous asymptotic expansion of the buoyancy moment that preserves all third-order terms, enabling a consistent description of moderately large-amplitude oscillations under wave-induced parametric excitation.

3. Equations of motion

This section summarizes the contributions illustrated in the previous section to obtain the equations of motion, that will be solved in the subsequent sections by two different analytical methods.

The equations of motion of the 2-DOF system of Fig. 1(a) are obtained by considering all the contributions explained in Section 2 and by adding the inertial terms and the damping, which is assumed to be linear (more complex expressions of damping are left for future works):

$$\begin{aligned} &I_T \ddot{\vartheta}_T + C_T(\dot{\vartheta}_T - \dot{\vartheta}_P) - c_1 \vartheta_T + c_2 \vartheta_T^3 \\ &+ K_1(\vartheta_T - \vartheta_P) + K_3(\vartheta_T - \vartheta_P)^3 = 0, \end{aligned} \tag{14}$$

$$\begin{aligned} &I_P \ddot{\vartheta}_P + C_P \dot{\vartheta}_P + C_T(\dot{\vartheta}_P - \dot{\vartheta}_T) + [c_3 + c_4\eta(t) + c_5\eta(t)^2]\vartheta_P \\ &+ [c_6 + c_7\eta(t) + c_8\eta(t)^2]\vartheta_P^3 + K_1(\vartheta_P - \vartheta_T) + K_3(\vartheta_P - \vartheta_T)^3 = 0, \end{aligned} \tag{15}$$

where

$$\begin{aligned} &c_1 = K_{\mathrm{MT}}, \quad c_2 = \frac{K_{\mathrm{MT}}}{6}, \quad c_3 = K_{\mathrm{MP}} - \rho\, g\, A_P \left(\frac{H_s^2}{2} + H_s h_s \right), \\ &c_4 = -\rho\, g\, A_P h_s, \quad c_5 = \frac{\rho\, g\, A_P}{2}, \\ &c_6 = -\frac{K_{\mathrm{MP}}}{6} + \rho\, g\, A_P \left(\frac{H_s^2}{12} + \frac{H_s h_s}{6} + \frac{h_s^2}{2} \right), \\ &c_7 = -\frac{5\,\rho\, g\, A_P h_s}{6}, \quad c_8 = \frac{5\,\rho\, g\, A_P}{12}, \end{aligned} \tag{16}$$

and where I_T and I_P are the tower and the spar platform mass moments of inertia with respect to the point O, respectively, and C_T and C_P are the linear damping coefficients for the tower and the spar platform, respectively.

Table 1 reports the parameters of the model considered as a reference (but the analytical approach of course is valid for any parameters).

In particular, as for the tower's data, the NREL 5-MW reference wind turbine [52] has been considered. Instead, with regard to the spar platform, the OC3 Hywind model in parked condition [53] has been adopted as a baseline for the platform properties. However, the

Table 1
Parameters of the mechanical system.

Parameter	Value	Dimension
I_T	3 511 782 090	kg m^2
I_P	78 788 250 000	kg m^2
K_1	7 186 690 018.31	N m
K_3	7 918 505 408.22	N m
c_1	441 450 000	N m
c_2	73 575 000	N m
c_3	467 739 524.7	N m
c_4	−3 852 387	N
c_5	385 238.7	N/m
c_6	−68 325 619.95	N m
c_7	−3 210 322.5	N
c_8	321 032.25	N/m

original OC3 'platform system' is defined together with its station-keeping system, i.e., the catenary mooring arrangement that prevents the floater from drifting and contributes to the global rigid-body mass properties of the assembly. In the present reduced-order model, the low-frequency station-keeping role of the moorings is represented kinematically by constraining the platform reference hinge O to be fixed in space (surge and heave are neglected), so that the structure cannot translate and only pitch is retained. As a consequence, the mooring restoring forces and their dynamic coupling with platform motions are not modeled explicitly. Nevertheless, mooring lines and associated components such as clump weights are an integral part of the OC3 spar system and are intentionally designed to affect the global stability by adding mass and inertia and by lowering the overall center of gravity. Therefore, using the OC3 data without modifications would be inconsistent with the present modeling hypotheses. For this reason, the OC3 mass properties have been adjusted by removing the mooring-system contribution and recomputing consistently the platform-system mass m_P, the location of the center of mass G_P, and the moment of inertia I_P around O, using standard mass-weighted averages and parallel-axis relations. Physically, neglecting the moorings reduces the total mass and moment of inertia and shifts the platform-system center of gravity upward, which affects the pitch natural frequency and consequently the quantitative location of the parametric-resonance region. However, the hydrostatic parametric modulation mechanism investigated here is preserved, as it depends on the spar geometry and wave elevation.

3.1. The 1-DOF case

Let us consider the 1-DOF case that is obtained by assuming $\vartheta_T = \vartheta_P$, which is reasonable when K_1 and K_3 are large enough. Summing up (14) and (15) we obtain

$$I\ddot{\vartheta}_P + C_P\dot{\vartheta}_P + [c_9 + c_4\eta(t) + c_5\eta(t)^2]\vartheta_P + [c_{10} + c_7\eta(t) + c_8\eta(t)^2]\vartheta_P^3 = 0, \tag{17}$$

where $I = I_T + I_P$, $c_9 = c_3 - c_1$ and $c_{10} = c_2 + c_6$. Note that we need $c_9 > 0$, i.e. $c_3 > c_1$, to have that the rest position is stable without excitation, namely no static overturning.

With the values of Table 1 we have $c_3 > c_1$, and (17) reduces to

$$\begin{aligned}\ddot{\vartheta}_P = &-0.03574549870\,\xi\,\dot{\vartheta}_P \\ &- [0.0003194351695 - 0.00004680905830\,W\cos(\omega t) \\ &+ 0.000004680905830\,W^2\cos^2(\omega t)]\vartheta_P \\ &- [0.00006378345083 - 0.00003900754858\,W\cos(\omega t) \\ &+ 0.000003900754858\,W^2\cos^2(\omega t)]\vartheta_P^3,\end{aligned} \tag{18}$$

where the damping coefficient ξ is implicitly defined by $C_P = 2\xi\sqrt{Ic_9}$.

4. The multiple time scales method

In this section the approximate analytical expressions of period-2 *resonant* solutions of (17) are searched using the Multiple Time Scales Method (MTSM) [54]. They are sought in the form

$$\vartheta_P(t) = \varepsilon\vartheta_{P1}(T_0,T_2,T_4) + \varepsilon^3\vartheta_{P3}(T_0,T_2,T_4) + \varepsilon^5\vartheta_{P5}(T_0,T_2,T_4) + \dots, \tag{19}$$

where $T_i = \varepsilon^i t$, $i > 1$, are the slow times and $T_0 = t$ is the physical time, so that $\frac{d}{dt} = \frac{\partial}{\partial T_0} + \varepsilon^2\frac{\partial}{\partial T_2} + \varepsilon^4\frac{\partial}{\partial T_4}$. We also assume $C_P = \varepsilon^2 C_{P0}$ and $W = \varepsilon^2$, an expression that gives a physical meaning to the small parameter ε.

We follow the same approach as in Sect. 5.7.3 of [54]. With respect to the analysis reported therein, the elements of novelty of this work are that (i) the parametric excitation is also on the cubic term, (ii) there is also a quadratic term $\eta(t)^2$ in the parametric excitation, and (iii) we will also determine the fifth order solution, which is necessary to see some dynamical phenomena that cannot be seen up to the third order only.

Inserting (19) in (17), and collecting growing powers of ε, we obtain a sequence of problems, that are discussed and solved in the following.

4.1. First order problem

The first order problem is

$$I\frac{\partial^2\vartheta_{P1}}{\partial T_0^2} + c_9\vartheta_{P1} = 0, \tag{20}$$

and the solution is written in the complex variable form

$$\vartheta_{P1} = A(T_2,T_4)e^{i\Omega T_0} + \bar{A}(T_2,T_4)e^{-i\Omega T_0}, \tag{21}$$

where i is the imaginary unit and the bar means complex conjugate. The natural (circular) frequency is given by $\Omega = \sqrt{c_9/I}$. With the values of Table 1 we have $\Omega = 0.01787274935$ rad/s.

4.2. Second order problem

By the considered assumptions, the second order problem is automatically satisfied.

4.3. Third order problem

Before proceeding to the study of the third order problem, we have to select which PR we are interested in. We will consider the main one, i.e. $\omega \approx 2\Omega$. To quantify this closeness we introduce the detuning parameter σ such that $\omega = 2\Omega + \varepsilon^2\sigma$. This implies that $\omega t = 2\Omega t + \varepsilon^2 t\sigma = 2\Omega T_0 + \sigma T_2$.

The third order problem is then (g_P is given in Appendix A)

$$I\frac{\partial^2\vartheta_{P3}}{\partial T_0^2} + c_9\vartheta_{P3} + g_P = 0. \tag{22}$$

The solvability condition $\int_0^T g_P e^{-i\Omega T_0}dT_0 = 0, T = \frac{2\pi}{\Omega}$ gives

$$3c_{10}A^2\bar{A} + iC_{P0}\Omega A + 2iI\Omega\frac{\partial A}{\partial T_2} + \frac{c_4}{2}\bar{A}e^{i\sigma T_2} = 0. \tag{23}$$

The third order solution is then given by

$$\theta_{P3} = \frac{1}{16\,c_9}\left[2c_{10}(A^3e^{3i\Omega T_0} + \bar{A}^3e^{-3i\Omega T_0}) + c_4(Ae^{i(3\Omega T_0+\sigma T_2)} + \bar{A}e^{-i(3\Omega T_0+\sigma T_2)})\right]. \tag{24}$$

We now introduce real variables, i.e. we assume $A(T_2) = \frac{a(T_2)}{2}e^{i\phi(T_2)}$. Substituting in (23) and multiplying by $e^{i\phi(T_2)}$ we obtain

$$-I\Omega a\frac{d\phi}{dT_2} + \frac{3}{8}c_{10}a^3 + \frac{1}{2}iC_{P0}\Omega a + iI\Omega\frac{da}{dT_2} + \frac{1}{4}c_4 a e^{-i(2\phi-\sigma T_2)} = 0, \tag{25}$$

whose real and imaginary parts are

$$I\Omega\frac{da}{dT_2}+\frac{1}{2}C_{P0}\Omega a+\frac{1}{4}c_4 a\sin(\sigma T_2-2\phi)=0, \tag{26}$$

$$-I\Omega a\frac{d\phi}{dT_2}+\frac{3}{8}c_{10}a^3+\frac{1}{4}c_4 a\cos(\sigma T_2-2\phi)=0. \tag{27}$$

Obviously, there is the trivial solution $a=0$, which physically corresponds to the rest position. To check where it loses stability by a (Hopf) bifurcation, and to study possible other solutions, we consider the stationary solution (that corresponds to a periodic solution in the real system)

$$a(T_2)=a_0,\quad \phi(T_2)=\frac{\sigma T_2+\beta_0}{2}, \tag{28}$$

so that from (26) and (27) we get

$$\sin\beta_0=\frac{2C_{P0}\Omega}{c_4},\quad \cos\beta_0=\frac{4I\Omega\sigma-3c_{10}a_0^2}{2c_4}. \tag{29}$$

From

$$\tan\beta_0=\frac{4C_{P0}\Omega}{4I\Omega\sigma-3c_{10}a_0^2} \tag{30}$$

we can compute the constant phase angle β_0, which is independent of c_4 and which vanishes in the absence of damping, $C_{P0}=0$. From $\cos^2\beta_0+\sin^2\beta_0=1$ we obtain

$$c_4^2=\left(2I\Omega\sigma-\frac{3}{2}c_{10}a_0^2\right)^2+(2C_{P0}\Omega)^2, \tag{31}$$

which is the relation between c_4, σ and a_0 for having a periodic solution in the original system. Multiplying (31) by ε^4 it is possible to go back to the physical variables:

$$(Wc_4)^2=\left[2I\Omega(\omega-2\Omega)-\frac{3}{2}c_{10}\,aa_0^2\right]^2+(2C_P\Omega)^2, \tag{32}$$

where $aa_0=\varepsilon a_0$ is the (first order) physical amplitude of the response:

$$\vartheta_P(t)=\varepsilon a_0\cos\left(\frac{\omega t+\beta_0}{2}\right)+\dots. \tag{33}$$

4.4. Fourth order problem

By the considered assumptions, the fourth order problem is automatically satisfied.

4.5. Fifth order problem

By studying the fifth order problem, it is possible to see the effect of c_5 and c_7 in (17), which is an element of novelty with respect to the standard PR analysis of a Duffing equation.

The fifth order problem is (h_P is given in Appendix A)

$$I\frac{\partial^2\vartheta_{P5}}{\partial T_0^2}+c_9\vartheta_{P5}+h_P=0. \tag{34}$$

The solvability condition $\int_0^T h_P e^{-i\Omega T_0}dT_0=0, T=\frac{2\pi}{\Omega}$ gives

$$\begin{aligned}&I\frac{\partial^2 A}{\partial T_2^2}+2iI\Omega\frac{\partial A}{\partial T_4}+C_{P0}\frac{\partial A}{\partial T_2}+\frac{c_4c_{10}A^3}{16c_9}e^{-i\sigma T_2}+\frac{c_4^2A}{32c_9}+\frac{c_5A}{2}\\&+\frac{3c_{10}^2\bar{A}^2A^3}{8c_9}+\frac{3c_4c_{10}A\bar{A}^2}{16c_9}e^{i\sigma T_2}+\frac{c_7A^3}{2}e^{-i\sigma T_2}+\frac{3c_7A\bar{A}^2}{2}e^{i\sigma T_2}=0.\end{aligned} \tag{35}$$

The term $\frac{\partial A}{\partial T_2}$ is given by (23):

$$\frac{\partial A}{\partial T_2}=\frac{1}{2I\Omega}\left(3ic_{10}A^2\bar{A}+\frac{1}{2}ic_4\bar{A}e^{i\sigma T_2}-C_{P0}\Omega A\right). \tag{36}$$

The derivative $\frac{\partial A}{\partial T_4}$ is computed in the Appendix B and is given by (B.5).

As explained in Section 4, the derivative of the amplitude A with respect to physical time t is

$$\frac{dA}{dt}=\frac{\partial A}{\partial T_0}+\varepsilon^2\frac{\partial A}{\partial T_2}+\varepsilon^4\frac{\partial A}{\partial T_4}=\varepsilon^2\frac{\partial A}{\partial T_2}+\varepsilon^4\frac{\partial A}{\partial T_4}, \tag{37}$$

where use is made of $\frac{\partial A}{\partial T_0}=0$, see (21). We have that

$$\varepsilon A(t)=\frac{\varepsilon a(t)}{2}e^{i\phi(t)}=\frac{aa(t)}{2}e^{i\phi(t)}, \tag{38}$$

where $aa(t)=\varepsilon a(t)$ is the physical amplitude of the first order solution, see (33). Furthermore, let us define $\beta(t)$ implicitly by

$$\phi(t)=\frac{\sigma\sigma\, t+\beta(t)}{2},\quad \sigma\sigma=\varepsilon^2\sigma=\omega-2\Omega. \tag{39}$$

Based on the previous developments, we have

$$\begin{aligned}&\frac{1}{2}\frac{d\,aa(t)}{dt}+\frac{i}{4}aa(t)\frac{d\,\beta(t)}{dt}+\frac{i}{4}aa(t)\varepsilon^2\sigma\\&=\frac{d(\varepsilon A)}{dt}e^{-i\phi(t)}=\left(\varepsilon^3\frac{\partial A}{\partial T_2}+\varepsilon^5\frac{\partial A}{\partial T_4}\right)e^{-i\phi(t)}.\end{aligned} \tag{40}$$

By inserting (36) and (B.5) in (40) and separating the real and imaginary parts we obtain, after several computations and remembering that $W=\varepsilon^2$:

$$\begin{aligned}&-512\,I\,\Omega\,c_9^2\frac{d\,aa(t)}{dt}\\&+[(-64\,I\,\Omega\,\sigma\sigma+128c_9)Wc_4c_9\sin(\beta(t))-256C_P\Omega c_9^2]aa(t)\\&+[(-40Wc_4c_9c_{10}+64Wc_7c_9^2)\sin(\beta(t))+96C_Pc_9c_{10}\Omega]aa(t)^3=0,\end{aligned} \tag{41}$$

$$\begin{aligned}&\Big[-64(I\Omega\sigma\sigma-2c_9)Wc_4c_9\cos(\beta(t))-256I\Omega\sigma\sigma c_9^2+128W^2c_5c_9^2\\&+24(Wc_4)^2c_9-\frac{64c_9^2C_P^2}{I}+256I\Omega c_9^2\frac{d\,\beta(t)}{dt}\Big]aa(t)\\&+[(16Wc_4c_9c_{10}+128Wc_7c_9^2)\cos(\beta(t))+192c_9^2c_{10}]aa(t)^3\\&-30c_9c_{10}^2aa(t)^5=0.\end{aligned} \tag{42}$$

In (42) it is notable the presence of the $aa(t)^5$, which cannot be seen by the third order analysis.

Similarly to (28) we now look for stationary solutions, i.e.

$$aa(t)=aa_0,\quad \beta(t)=\beta_0. \tag{43}$$

Inserting (43) in (41) and (42), we obtain

$$\sin\beta_0=\frac{4C_P\Omega(8c_9-3c_{10}aa_0^2)}{W\left[(8c_7c_9-5c_4c_{10})aa_0^2-8c_4c_9\left(\frac{\sigma\sigma}{\Omega}-2\right)\right]}, \tag{44}$$

$$\cos\beta_0=\frac{15c_{10}^2aa_0^4-96c_9c_{10}aa_0^2+128c_9^2\frac{\sigma\sigma}{\Omega}+32(C_P\Omega)^2-W^2(64c_5c_9+12c_4^2)}{8W\left[(8c_7c_9+c_4c_{10})aa_0^2-4c_4c_9\left(\frac{\sigma\sigma}{\Omega}-2\right)\right]}. \tag{45}$$

From

$$\sin^2\beta_0+\cos^2\beta_0=1 \tag{46}$$

we obtain a sixth order *algebraic* equation in aa_0^2. Thus, we can have up to six different solutions, depending on the various parameters. This equation is quite complex, but can be managed (and solved) by a symbolic manipulation software. Meaningful examples are reported in Section 6. In the absence of damping, $C_P=0$, it simplifies to $\cos(\beta_0)=\pm1$, which is second order in aa_0^2. Thus, we can have up to four solutions in this limit case.

Once aa_0 has been determined, the phase angle β_0 is given by

$$\beta_0=\arctan\left(\frac{\sin\beta_0}{\cos\beta_0}\right), \tag{47}$$

while the solution up to the third order is

$$\begin{aligned}\vartheta_P(t)=&aa_0\cos\left(\frac{\omega t+\beta_0}{2}\right)+aa_0\frac{Wc_4}{16c_9}\cos\left(\frac{3\omega t+\beta_0}{2}\right)\\&+aa_0^3\frac{c_{10}}{32c_9}\cos\left(\frac{3\omega t+3\beta_0}{2}\right)+\dots.\end{aligned} \tag{48}$$

5. The harmonic balance method

In the previous section, *resonant* period-2 (i.e. with frequency $\omega/2$) solutions are considered. To analytically detect *non-resonant* period-1 (i.e. with frequency ω) solutions, the harmonic balance method is herein applied.

In recent years, the HBM has undergone substantial methodological advances, consolidating its role as a reference framework for efficiently computing nonlinear periodic solutions and their stability in forced and parametrically excited systems. Modern formulations emphasize systematic multi-harmonic expansions, robust algebraic solvers, and improved strategies to handle strong nonlinearities and large-scale models, thereby extending the applicability of HBM well beyond classical single-harmonic settings [55]. A comprehensive and implementation-oriented perspective on HBM for nonlinear vibration problems is provided by the monograph of Krack and Gross [56], which also clarifies the connections between classical frequency-domain HBM and modern continuation workflows. Recent research has further strengthened these links by introducing collocation-based "reconstruction" frameworks that explicitly diagnose and suppress aliasing, thereby enabling very high-order, non-aliasing multi-harmonic solutions and a clearer equivalence between frequency- and time-domain harmonic analyses [57]. In parallel, scalable formulations have been proposed for high-dimensional nonlinear models, including general HBM implementations and variants that combine harmonic balance with dimension-reduction and FFT-based acceleration to make large-scale periodic-response computations tractable [58,59]. At the workflow level, HBM is increasingly coupled with robust continuation strategies such as ANM–HBM to reliably trace solution branches (including strongly nonlinear regimes), while automatic-differentiation-enhanced formulations automate Jacobian evaluation within Newton-type solvers, improving robustness and usability for complex nonlinearities and large-scale systems [60,61]. Beyond single-frequency periodic responses, recent extensions address multi-frequency and quasi-periodic dynamics via reconstruction multiple-harmonic-balance approaches, and computational efficiency is further improved by adaptive harmonic-selection strategies, that retain only the most relevant harmonics without sacrificing accuracy [62,63].

In the offshore renewable-energy context, HBM-based analyses have been increasingly adopted to map nonlinear harmonic resonances, jump phenomena, and bifurcations in reduced-order models of FOWTs and their subsystems. In this direction, HBM has been used to characterize coupled surge–heave dynamics in TLP-type FOWTs and to track harmonic resonance scenarios and bifurcation patterns [64]. Likewise, recent spar-buoy studies exploit HBM as a computational backbone to obtain steady-state responses and stability trends when introducing strongly nonlinear vibration-mitigation devices and to support systematic parameter tuning [65,66]. In parallel, HBM has been specifically tailored to compute the nonlinear periodic response of mooring cables, providing an efficient route to capture periodic solutions and their dependence on excitation and system parameters [67,68]. Finally, the integration of HBM within optimization loops for nonlinear absorbers further illustrates the current trend toward HBM-driven design workflows in complex engineering applications [69].

The approximate solution of (17) is now sought after in the form

$$\vartheta_P(t) = b_0 + b_{1c}\cos(\omega t) + b_{1s}\sin(\omega t) = b_0 + aa_0\cos(\omega t + \beta_0), \tag{49}$$

where b_0, b_{1c} and b_{1s} are the three unknowns, $aa_0 = \sqrt{b_{1c}^2 + b_{1s}^2}$ the amplitude and $\beta_0 = -\arctan(b_{1s}/b_{1c})$ the phase.

Inserting (49) in (17), expanding and setting equal to zero the constant term and the coefficients of $\cos(\omega t)$ and $\sin(\omega t)$, we obtain the following three algebraic nonlinear equations:

$$\begin{aligned}
&\left[4\,c_8\,b_0^2 + 4\,c_5 + \left(9\,b_{1c}^2 + 3\,b_{1s}^2\right)c_8\right]b_0 W^2 \\
&+ \left[4\,c_4 + \left(12\,b_0^2 + 3(b_{1c}^2 + b_{1s}^2)\right)c_7\right]b_{1c} W \\
&+ \left[\left(8\,b_0^2 + 12\,(b_{1c}^2 + b_{1s}^2)\right)c_{10} + 8\,c_9\right]b_0 = 0, \qquad (50)\\
&\left[2\,c_5 + \left(6\,b_0^2 + b_{1s}^2 + 3\,b_{1c}^2\right)c_8\right]b_{1s} W^2 + 12\,c_7\,b_0\,b_{1c}\,b_{1s} W \\
&+ 6\left(4\,b_0^2 + b_{1c}^2 + b_{1s}^2\right)b_{1s}c_{10} - 8\,C_P\,b_{1c}\,\omega + 8\,(c_9 - I\omega^2)\,b_{1s} = 0, \qquad (51)\\
&\left[6\,c_5 + \left(18\,b_0^2 + 3\,b_{1s}^2 + 5\,b_{1c}^2\right)c_8\right]b_{1c} W^2 \\
&+ \left[8\,c_4 + \left(8\,b_0^2 + 6\,b_{1s}^2 + 18\,b_{1c}^2\right)c_7\right]b_0 W \\
&+ \left(24\,b_0^2 + 6(b_{1c}^2 + b_{1s}^2)\right)b_{1c}c_{10} + 8\,C_P\,b_{1s}\,\omega + 8\,(c_9 - I\omega^2)\,b_{1c} = 0. \qquad (52)
\end{aligned}$$

They can be solved numerically, and then the approximate analytical solutions obtained.

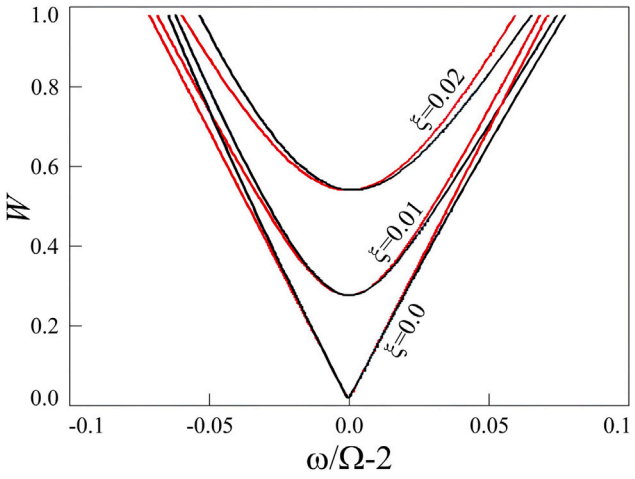

Fig. 2. The Ince-Strutt bifurcation diagram for different values of the damping coefficient ξ. Black is the fifth order MTSM solution, red the third order MTSM solution. Above the reported thresholds the rest position is unstable, below it is stable.

6. Results and discussion

To illustrate the results provided by the MTSM and the HBM, we consider the values of the parameters reported in Table 1, i.e. we consider a realistic case, so that the outcomes are of immediate applicability, even for FOWTs similar to the specific one considered in this section.

There are only three governing parameters, ω, W, and ξ, which will be varied in the sequel.

We initially determine the bifurcation in the excitation frequency-excitation amplitude parameter space, known as the Ince-Strutt diagram (see, for example, Fig. 5.9 of [54]). This is obtained by inserting $aa_0 = 0$ in (46) (fifth order MTSM) and in (32) (third order MTSM). As shown in Fig. 2, the instability region (above the curves) has the classical V-shape, and there are only minor qualitative changes, in particular for large excitation amplitude W. The fifth order curves lose symmetry with respect to the axis $\sigma\sigma = 0$.

6.1. Excitation frequencies larger than the resonant one

As a representative case of frequencies larger than the resonant one in this subsection we consider $\sigma\sigma/\Omega = 0.07$.

To better visualize the effect of damping, let us define $\mu = 1/\xi$. The solution $aa_0(\mu)$ is depicted in Fig. 3(a), (c) and (e) for different values of the sea wave excitation amplitude W.

It is seen that the loss of stability of the rest solution $aa_0 = 0$ occurs by means of a *subcritical* Hopf bifurcation, creating a period-2 solution. The zooms of Fig. C.7(a), (c) and (e) show that there are significant quantitative differences between the third and the fifth order MTSM solutions. Furthermore, although the third order approximation is still able to capture the qualitative behavior for low values of aa_0

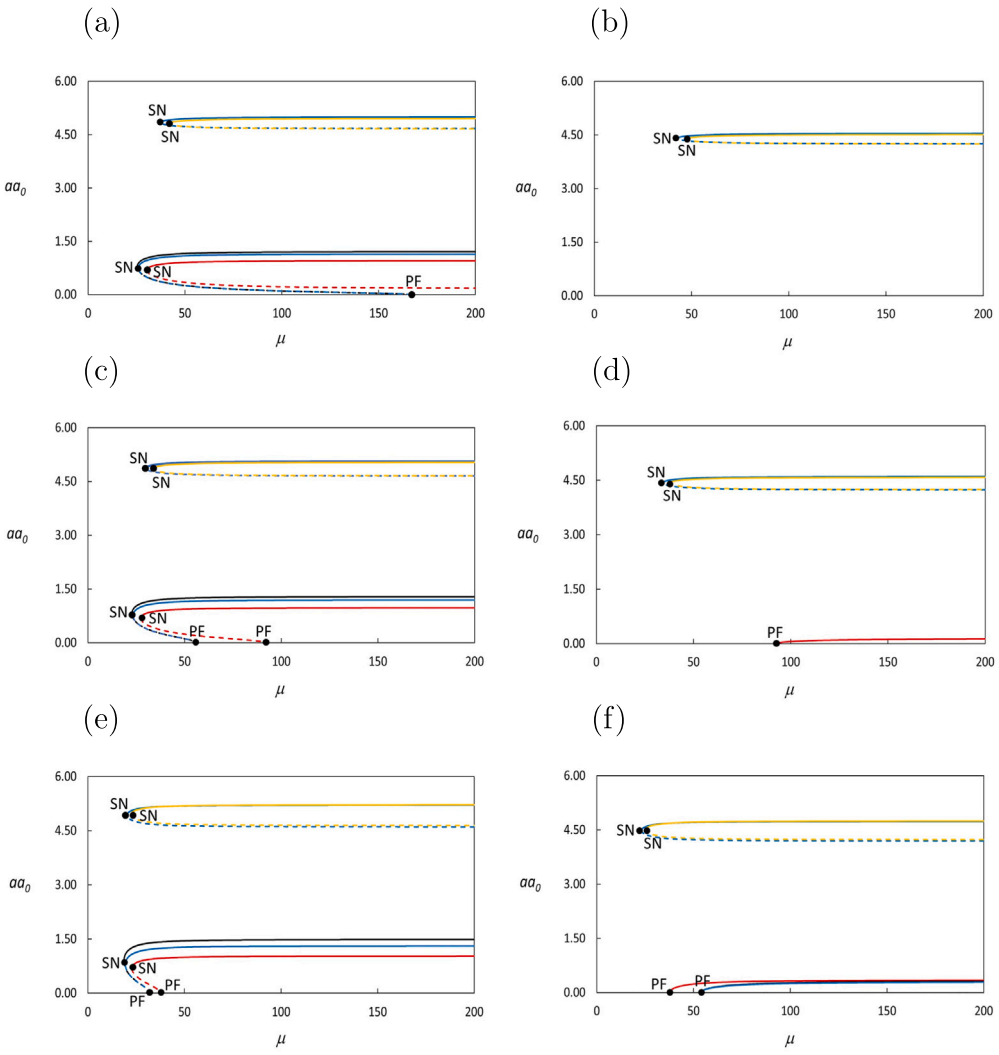

Fig. 3. The solutions $aa_0(\mu)$ for (a) $\sigma\sigma/\Omega = 0.07$ (i.e. $\omega = 0.03699659115$ rad/s) and $W = 0.9$ m; (c) $\sigma\sigma/\Omega = 0.07$ and $W = 1$ m; (e) $\sigma\sigma/\Omega = 0.07$ and $W = 1.2$ m; (b) $\sigma\sigma/\Omega = -0.07$ (i.e. $\omega = 0.03449440625$ rad/s) and $W = 0.9$ m; (d) $\sigma\sigma/\Omega = -0.07$ and $W = 1$ m; (f) $\sigma\sigma/\Omega = -0.07$ and $W = 1.2$ m. Black is the fifth order period-2 MTSM solutions, red the third order period-2 MTSM solutions, yellow the period-1 HBM solutions, blue the numerical solutions. Continuous lines are the stable paths, dashed lines the unstable paths. Zooms of figures (a), (c) and (e) are reported in Fig. C.7. Zooms of figures (b), (d) and (f) are reported in Fig. C.9.

in Fig. C.7(c) (i.e. when $W = 1$ m) and Fig. C.7(e) (i.e. when $W = 1.2$ m), it becomes inadequate in Fig. C.7(a) (i.e. when $W = 0.9$ m), because the subcritical Hopf bifurcation phenomenon is lost. In this case, the third-order solution actually indicates that the unstable path is always detached from the rest position and asymptotically approaches a constant value of aa_0 as $\mu \to \infty$ (i.e. $\xi \to 0$). This aspect makes the fifth order solution necessary, as it is always able to capture the subcritical Hopf bifurcation phenomenon. As a matter of fact, the numerical solution confirms this behavior, showing an excellent correspondence with the fifth order unstable paths, although small quantitative differences appear in the stable paths.

The true element of novelty can be appreciated in the full views of Fig. 3(a), (c) and (e). In fact, for large values of aa_0 there is a new separate branch of period-1 solutions, with a stable and an unstable path, ensuing from a Saddle-Node (SN) bifurcation, that is totally lost by both the third and fifth order MTSM analyses. In this case, instead, only the HBM is able to analytically detect the new family of large-amplitude solutions. In Fig. C.7(b), (d) and (f) the HBM curves show an excellent agreement with the numerical path following results, in spite of some small quantitative differences, which are acceptable for high values of aa_0. This confirms the accuracy of the theoretical HBM predictions in this range.

To further verify the existence of these new solutions, we report in Fig. 4(a) the basins of attraction for $W = 1$ m and $\mu = 40$ (i.e. $\xi = 0.025$). The large-amplitude solution not only exists, but indeed they are two distinct solutions with a phase shift of half a period (and with the same amplitude, this is why they overlap in Figs. 3 and 6). These new solutions have quite a large basins of attraction (greens), that bound the extension of the basin of the small amplitude oscillation (red) and of the rest position (blue). Thus, they are quite important from a practical point of view, since they can limit the robustness of the small amplitude oscillations, possibly leading to unwanted and unexpected failure of the system when the perturbations on real structure are large enough to reach the basins of these large amplitude solutions.

As a matter of fact, we note that in the present case the rest solution is still stable, but has a basin that is so tiny as to be easily

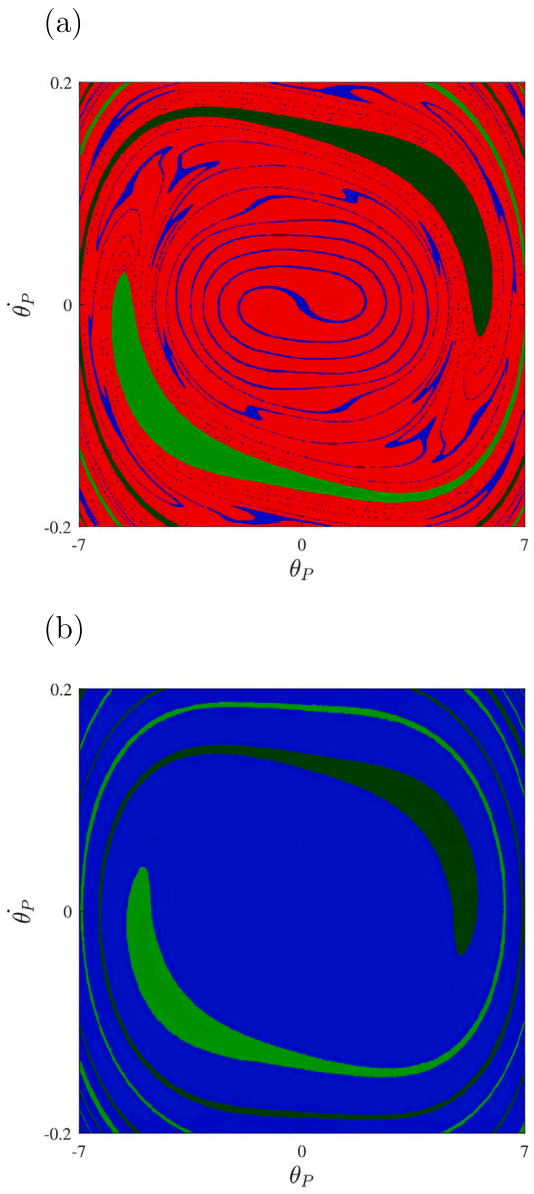

Fig. 4. Basins of attraction for (a) $\sigma\sigma/\Omega = 0.07$ (i.e. $\omega = 0.03699659115$ rad/s), $\mu = 40$ (i.e. $\xi = 0.025$), $W = 1$ m and (b) $\sigma\sigma/\Omega = -0.07$ (i.e. $\omega = 0.03449440625$ rad/s), $\mu = 50$ (i.e. $\xi = 0.02$), $W = 1$ m. Blue is the rest solution, red the small amplitude period-2 solution, dark and light green the large amplitude period-2 oscillations.

overcome by small perturbations and uncertainties, thus leading to *practical instability* [70].

In Fig. 5 the time histories and the phase portraits of the numerical solutions shown in Fig. 4(a) are reported, further confirming the analytical results shown in Fig. 3(a), (c) and (e), in particular in terms of the periodicity of the solutions.

To get the curves in Fig. 5, the equation of motion (18) has been numerically integrated in *Python* with the scientific library *SciPy*. In particular, the problem has been formulated as an initial value problem for a first-order system of ordinary differential equations and solved using the `solve_ivp` function from the `scipy.integrate` subpackage, which numerically integrates $\dot{y} = f(t, y)$, starting from $y(t_0) = y_0$. The implicit 5-order Runge–Kutta solver *Radau* has been employed, which is specifically designed for stiff or nonlinear problems and long-time integrations. The system has been integrated in the time domain from $t = 0$ to $t = 800000$ s, to ensure complete decay of transients and convergence to the asymptotic attractor. The time step has been chosen as $dt = T_0/1000$ (T_0 is the excitation period), which is essential to accurately resolve the oscillatory response (including subharmonic and higher-harmonic components) and to avoid sampling artifacts such as aliasing. The time histories reported in Fig. 5 correspond to the final window $t \in [7.9 \times 10^5, 8 \times 10^5]$ s, that has been renormalized for plotting. Different solutions have been obtained by varying the initial conditions in the numerical integration.

From an engineering perspective, this multiperiodicity is highly critical, because diagnostic tools or control algorithms, based only on dominant frequency or amplitude detection, may easily misinterpret a subharmonic period-2 response as a period-1 oscillation, leading to inadequate or even destabilizing corrective actions [71]. This scenario compromises system robustness and poses a risk of motions that are not anticipated by standard design criteria.

The subcritical Hopf bifurcation can also be observed in Fig. 6(a), (c) and (e), where the solution $aa_0(W)$ is shown for different values of the damping coefficient ξ. For each considered value of the damping ratio ξ, the rest solution $aa_0 = 0$ again loses stability through a subcritical Hopf bifurcation, giving rise to a resonant period-2 response associated with the main 2:1 PR. This unstable branch of small-amplitude oscillations is accurately captured by the MTSM curves; the corresponding behavior is illustrated in more detail in the zoomed views (a), (c) and (e) of Fig. C.8.

In parallel, as in Fig. 3(a), (c) and (e), the same bifurcation diagrams reveal the presence of an additional non-resonant period-1 solution, which does not bifurcate from the rest position but emerges instead as a detached branch at finite amplitude. This large-amplitude family is detected analytically only through the HBM and is confirmed by the numerical path-following results; its detailed evolution is shown in the zoomed panels (b), (d) and (f) of Fig. C.8. The blue curves in Figs. 6(a), (c) and (e) and C.8, corresponding to the numerical continuation, corroborate the existence of both the resonant period-2 and the non-resonant period-1 solutions. However, an important difference with respect to Fig. 3(a), (c) and (e) concerns the relative performance of the third- and fifth-order MTSM approximations. In Fig. 3(a), (c) and (e), the subcritical Hopf bifurcation associated with the period-2 response could be reliably reproduced only by the fifth-order expansion, whereas the third-order approximation was, in some cases, unable even to provide a qualitatively correct description of the unstable branch emerging from the rest state. In contrast, the curves in Fig. 6(a), (c) and (e) show that, when aa_0 is plotted with respect to W, the fifth-order MTSM solution mainly plays a refining role: it follows almost perfectly the numerically computed unstable branch and a substantial portion of the stable branch, deviating only slightly for large values of the excitation amplitude W. In this setting, the third-order MTSM approximation introduces essentially quantitative discrepancies with respect to both the fifth-order and the numerical results, but it still correctly reproduces the subcritical Hopf bifurcation mechanism and the overall topology of the resonant period-2 branch. Therefore, while the fifth-order correction is crucial to achieve quantitative accuracy along the entire bifurcation diagram, the third-order formulation already captures the essential qualitative features of the bifurcation phenomenon in Fig. 6(a), (c) and (e), unlike what happens in Fig. 3(a), (c) and (e).

6.2. Excitation frequencies smaller than the resonant one

As a representative case of frequencies smaller than the resonant one in this subsection we consider $\sigma\sigma/\Omega = -0.07$.

The solution $aa_0(\mu)$ for different values of the sea wave excitation amplitude W is illustrated in Fig. 3(b), (d) and (f). The first difference with respect to the previous case is that now the Hopf bifurcation is *supercritical*, and thus less dangerous from a practical point of view.

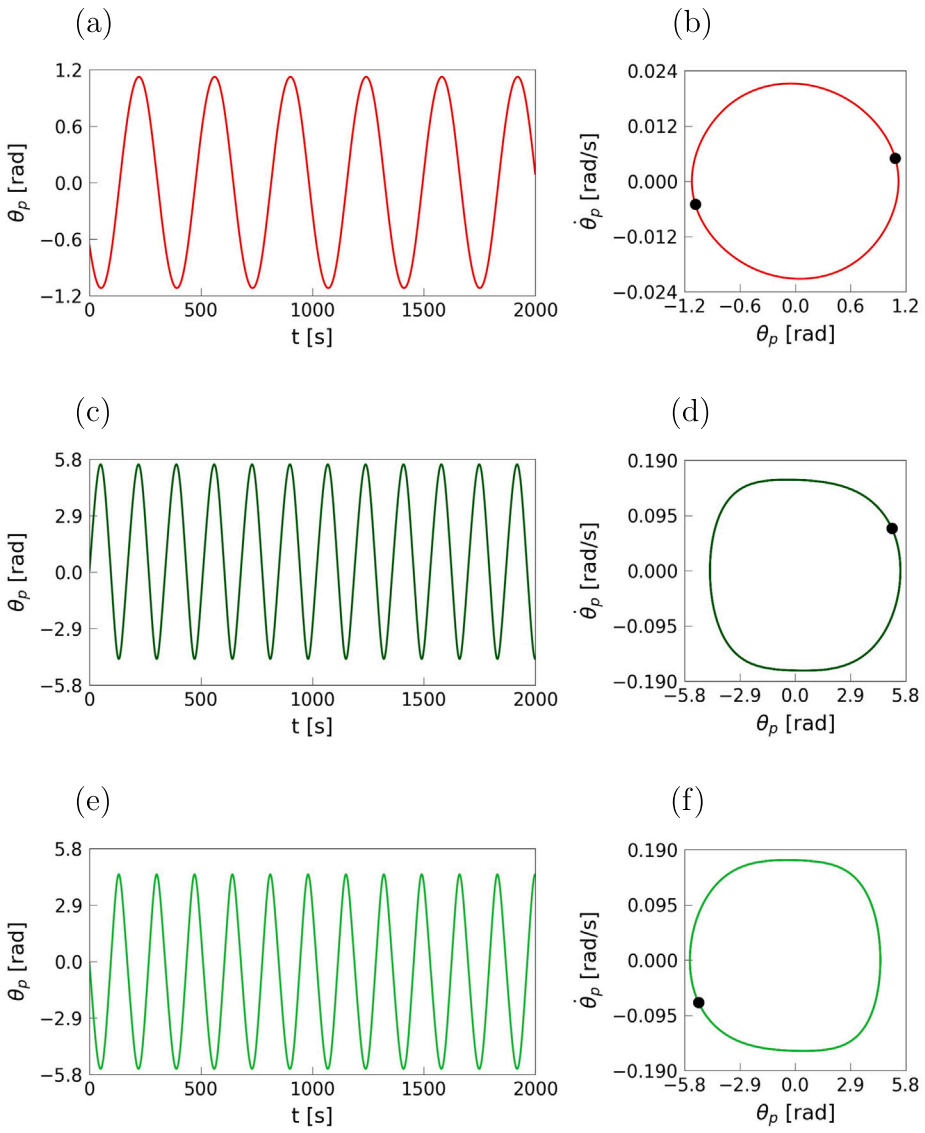

Fig. 5. The numerical periodic solutions for $\sigma\sigma/\Omega = 0.07$ (i.e. $\omega = 0.03699659115$ rad/s), $\xi = 0.025$ and $W = 1$ m, shown in Fig. 4(a). (a), (c) and (e) show time histories of $\vartheta_p(t)$ for $[\vartheta_p(0), \dot{\vartheta}_p(0)] = [1.086422$ rad, 0.004977 rad/s$]$, $[\vartheta_p(0), \dot{\vartheta}_p(0)] = [5.073689$ rad, 0.072870 rad/s$]$ and $[\vartheta_p(0), \dot{\vartheta}_p(0)] = [-5.073689$ rad, -0.072870 rad/s$]$. (b), (d) and (f) show phase portraits and Poincaré map points (black) for $[\vartheta_p(0), \dot{\vartheta}_p(0)] = [1.086422$ rad, 0.004977 rad/s$]$, $[\vartheta_p(0), \dot{\vartheta}_p(0)] = [5.073689$ rad, 0.072870 rad/s$]$ and $[\vartheta_p(0), \dot{\vartheta}_p(0)] = [-5.073689$ rad, -0.072870 rad/s$]$.

Moreover, this phenomenon is actually present only in the zoomed view of Fig. C.9(d), as it is shown by both the fifth-order and the numerical results. In contrast, in Fig. C.9(b) the small-amplitude solution is predicted by the third-order approximation, but not further confirmed by the numerical simulations, while in Fig. 3(b) it is completely absent. It follows that, when $W \leq 1$ m, the system admits only the large-amplitude solution, which represents the second important difference with respect to the case analyzed in Fig. 3(a), (c) and (e). However, the large-amplitude oscillations are still detected only by the HBM and are numerically checked by the path-following technique, despite some small acceptable quantitative differences already observed in the previous case.

To further confirm that the large amplitude oscillation is genuine, we report in Fig. 4(b) the basins of attraction for $W = 1$ m and $\mu = 50$ (i.e. $\xi = 0.02$). According to the bifurcation diagram of Fig. 3(d), it is seen that there are no longer the small amplitude oscillations, so that the large amplitude oscillations now delimit directly the basin of attraction of the rest solution, which can lose practical stability for large enough perturbations. Consistently, the basins in Fig. 4(b) further underscores the engineering criticality of the newly identified large-amplitude solution: it can persist within excitation-frequency intervals commonly regarded as safe. The analytical HBM results, therefore, prove to be essential, as they are able to discover the large-amplitude solution, which is indeed the only non-vanishing one actually existing in this scenario.

A complementary view of the same supercritical Hopf scenario is provided by Fig. 6(b), (d) and (f), where the response amplitude aa_0 is now plotted as a function of the excitation amplitude W for three different values of the damping ratio ξ. As pointed out in the zoomed view of Fig. C.10(a), (c) and (e), for each considered value of ξ, the

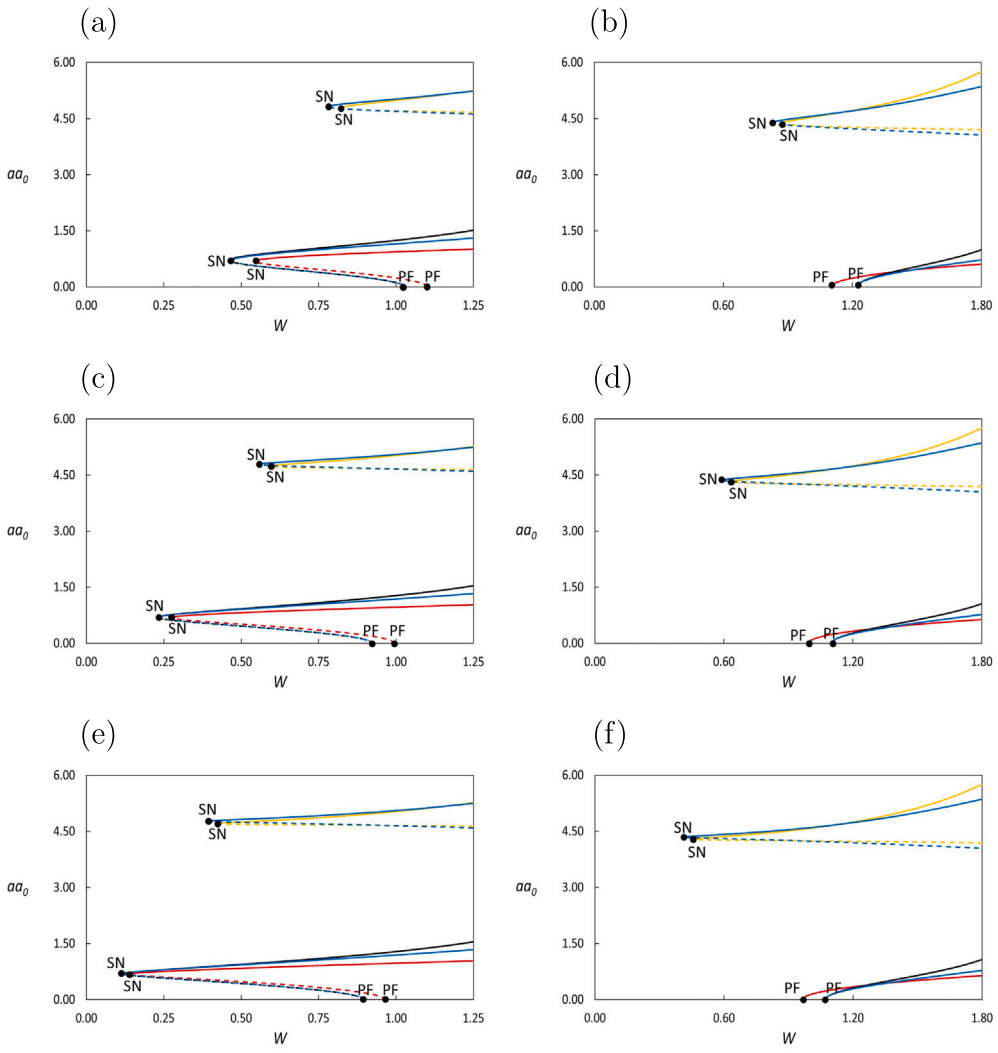

Fig. 6. The solutions $aa_0(W)$ for (a) $\sigma\sigma/\Omega = 0.07$ (i.e. $\omega = 0.03699659115$ rad/s) and $W = 0.9$ m; (c) $\sigma\sigma/\Omega = 0.07$ and $W = 1$ m; (e) $\sigma\sigma/\Omega = 0.07$ and $W = 1.2$ m; (b) $\sigma\sigma/\Omega = -0.07$ (i.e. $\omega = 0.03449440625$ rad/s) and $W = 0.9$ m; (d) $\sigma\sigma/\Omega = -0.07$ and $W = 1$ m; (f) $\sigma\sigma/\Omega = -0.07$ and $W = 1.2$ m. Black is the fifth order period-2 MTSM solutions, red the third order period-2 MTSM solutions, yellow the period-1 HBM solutions, blue the numerical solutions. Continuous lines are the stable paths, dashed lines the unstable paths. Zooms of figures (a), (c) and (e) are reported in Fig. C.8. Zooms of figures (b), (d) and (f) are reported in Fig. C.10.

rest solution $aa_0 = 0$ loses stability in favor of a stable small-amplitude period-2 oscillatory solution. The stable period-2 branch is captured both by the third order and the fifth order MTSM analyses. As expected, the latter is the only able to get closer to the numerical solution, showing an excellent agreement at the beginning, while departing only marginally at higher values of the excitation amplitude W. However, despite some quantitative differences, the third order approximation is always able to capture the qualitative behavior of the bifurcation phenomenon, unlike the scenario in Fig. 3(b), (d) and (f). In parallel, even in this case, the diagrams of Fig. C.10(b), (d) and (f) reveal the presence of a detached large-amplitude period-1 branch, obtained analytically only via the HBM and confirmed numerically, with a stable and unstable paths merging at a SN bifurcation. Consistently with the trends observed in Fig. 3(b), (d) and (f) and in the basin of Fig. 4(b), the curves in Fig. 6(b), (d) and (f) indicate that, at comparatively low excitation amplitudes W, the detached large-amplitude period-1 solution remains the only non-trivial attractor, while the resonant period-2 branch is not realized in practice.

7. Conclusions and future developments

This work investigated the wave-induced parametric response of a spar-type FOWT in pitch through a deliberately reduced analytical model, focusing on the primary 2:1 parametric-resonance condition. The study clarifies the bifurcation scenario, the coexistence of competing periodic attractors, and the implications for practical stability beyond classical linear checks.

From a modeling standpoint, a compact planar 2-DOF representation was developed and then reduced to a pitch-focused formulation to isolate the core instability mechanism. A third-order asymptotic expansion of the buoyancy overturning moment yielded explicit wave-elevation-dependent linear and cubic hydrostatic stiffness terms. This

provided a mechanistically consistent analytical basis for Mathieu-type pitch instability in spar platforms, while retaining the higher-harmonic content introduced by the wave-driven hydrostatic modulation.

On the methodological side, the primary 2:1 PR was treated via MTSM up to fifth order, enabling a systematic characterization of both subcritical and supercritical Hopf scenarios and explicitly showing when third-order approximations may become qualitatively insufficient. In parallel, a complementary Harmonic Balance formulation revealed a detached, non-resonant period-1 family at large amplitude, which cannot be captured by perturbation expansions around the rest state.

These analytical predictions were corroborated through numerical continuation, long-time direct integrations, and basin-of-attraction computations. The results confirmed the coexistence between small-amplitude resonant period-2 oscillations and detached large-amplitude period-1 attractors, and showed that the latter can exhibit wide basins within excitation and damping ranges commonly regarded as acceptable. Therefore, local stability and linear or low-order nonlinear assessments may systematically underestimate the risk of wave-induced large pitch motions.

Future work will extend the analysis to the full 2-DOF tower–pitch model to assess whether the additional DOF plays a relevant role, and will investigate further parametric resonances associated with the quadratic time-varying stiffness terms. In parallel, the reduced-order framework will be enriched by including heave, mooring-line effects, wind excitation, control and thermal effects, ultimately targeting a multi-DOF model under combined parametric (waves) and external (wind) excitation, as anticipated in [72], to better reflect the complexity of real FOWTs.

CRediT authorship contribution statement

Marco Luciani: Writing – review & editing, Writing – original draft, Software, Investigation, Formal analysis. **Stefano Lenci:** Writing – review & editing, Writing – original draft, Supervision, Methodology, Investigation, Funding acquisition, Formal analysis, Conceptualization.

Declaration of competing interest

The authors declare the following financial interests/personal relationships which may be considered as potential competing interests: Stefano Lenci reports financial support was provided by MUR. Stefano Lenci: Given his role as member of the Editorial Board Members, had no involvement in the peer review of this article and had no access to information regarding its peer review. Full responsibility for the editorial process for this article was delegated to another journal editor. If there are other authors, they declare that they have no known competing financial interests or personal relationships that could have appeared to influence the work reported in this paper.

Acknowledgments

This work has been developed as a part of the PRIN 2022 project "NonlinEar Phenomena in floaTing offshore wind tUrbiNEs (NEPTUNE)", prot. 2022W7SKTL, CUP I53D23001900006, funded by the Italian MUR. This support is gratefully acknowledged.

Appendix A. Some expressions

In this section we report some expressions that are used in the text.

The g_P term in the third order problem (22) takes the following expression:

$$g_P = \left(3c_{10}A^2\bar{A} + iC_{P0}\Omega A + 2iI\Omega\frac{\partial A}{\partial T_2} + \frac{c_4}{2}\bar{A}e^{i\sigma T_2}\right)e^{i\Omega T_0} + \left(3c_{10}\bar{A}^2A - iC_{P0}\Omega\bar{A} - 2iI\Omega\frac{\partial \bar{A}}{\partial T_2} + \frac{c_4}{2}Ae^{-i\sigma T_2}\right)e^{-i\Omega T_0} + \left(c_{10}A^3 + \frac{c_4}{2}Ae^{i\sigma T_2}\right)e^{3i\Omega T_0} + \left(c_{10}\bar{A}^3 + \frac{c_4}{2}\bar{A}e^{-i\sigma T_2}\right)e^{-3i\Omega T_0}, \tag{A.1}$$

The h_P term in the fifth order problem (34) takes the following expression:

$$h_P = I\left(\frac{\partial^2\vartheta_{P1}}{\partial T_2^2} + \frac{2\partial^2\vartheta_{P1}}{\partial T_0\partial T_4} + \frac{2\partial^2\vartheta_{P3}}{\partial T_0\partial T_2}\right) + C_{P0}\left(\frac{\partial\vartheta_{P1}}{\partial T_2} + \frac{\partial\vartheta_{P3}}{\partial T_0}\right) + c_4\ \vartheta_{P3}\cos(2\Omega T_0 + \sigma T_2) + c_5\ \vartheta_{P1}\cos^2(2\Omega T_0 + \sigma T_2) + 3\ c_{10}\ \vartheta_{P1}^2\ \vartheta_{P3} + c_7\ \vartheta_{P1}^3\cos(2\Omega T_0 + \sigma T_2). \tag{A.2}$$

Appendix B. Computation of $\frac{\partial A}{\partial T_4}$

Starting from the modulation equation (36), we first take its complex conjugate to obtain the equation for $\frac{\partial\bar{A}}{\partial T_2}$, and then differentiate (36) with respect to T_2 to derive the expression of $\frac{\partial^2 A}{\partial T_2^2}$. This yields:

$$\frac{\partial\bar{A}}{\partial T_2} = -\frac{1}{2I\Omega}\left(3ic_{10}A\bar{A}^2 + \frac{1}{2}ic_4Ae^{-i\sigma T_2} + C_{P0}\Omega\bar{A}\right), \tag{B.1}$$

$$\frac{\partial^2 A}{\partial T_2^2} = \frac{1}{2I\Omega}\left[-C_{P0}\Omega\frac{\partial A}{\partial T_2} + 3ic_{10}A\left(A\frac{\partial\bar{A}}{\partial T_2} + 2\bar{A}\frac{\partial A}{\partial T_2}\right) + \frac{1}{2}c_4\left(-\sigma\bar{A} + i\frac{\partial\bar{A}}{\partial T_2}\right)e^{i\sigma T_2}\right]. \tag{B.2}$$

Substituting (36) for $\frac{\partial A}{\partial T_2}$ and (B.1) for $\frac{\partial\bar{A}}{\partial T_2}$ into (B.2), and then collecting like terms, we obtain:

$$\frac{\partial^2 A}{\partial T_2^2} = \frac{1}{2I\Omega}\left[-\frac{C_{P0}}{2I}\left(3ic_{10}A^2\bar{A} + \frac{1}{2}ic_4\bar{A}e^{i\sigma T_2} - C_{P0}\Omega A\right) + \frac{3c_{10}A^2}{2I\Omega}\left(3c_{10}A\bar{A}^2 + \frac{1}{2}c_4Ae^{-i\sigma T_2} - iC_{P0}\Omega\bar{A}\right) - \frac{6c_{10}A\bar{A}}{2I\Omega}\left(3c_{10}A^2\bar{A} + \frac{1}{2}c_4\bar{A}e^{i\sigma T_2} + iC_{P0}\Omega A\right) - \frac{1}{2}c_4\sigma\bar{A}e^{i\sigma T_2} + \frac{c_4}{4I\Omega}\left(3c_{10}A\bar{A}^2e^{i\sigma T_2} + \frac{1}{2}c_4A - iC_{P0}\Omega\bar{A}e^{i\sigma T_2}\right)\right]. \tag{B.3}$$

Next, we rearrange the fifth-order solvability condition (35) and explicitly solve it for $\frac{\partial A}{\partial T_4}$, obtaining:

$$\frac{\partial A}{\partial T_4} = \frac{i}{2I\Omega}\left(I\frac{\partial^2 A}{\partial T_2^2} + C_{P0}\frac{\partial A}{\partial T_2} + \frac{c_4c_{10}A^3}{16c_9}e^{-i\sigma T_2} + \frac{c_4^2A}{32c_9} + \frac{c_5A}{2} + \frac{3c_{10}^2\bar{A}^2A^3}{8c_9} + \frac{3c_4c_{10}A\bar{A}^2}{16c_9}e^{i\sigma T_2} + \frac{c_7A^3}{2}e^{-i\sigma T_2} + \frac{3c_7A\bar{A}^2}{2}e^{i\sigma T_2}\right). \tag{B.4}$$

Finally, we replace $\frac{\partial A}{\partial T_2}$ and $\frac{\partial^2 A}{\partial T_2^2}$ in (B.4) with (36) and (B.3), respectively; after straightforward algebraic simplifications, this leads to the closed-form expression:

$$\frac{\partial A}{\partial T_4} = \frac{i}{32\,I^2\,\Omega^3}\left[(-4\Omega^2C_{P0}^2 - 24i\Omega c_{10}C_{P0}A\bar{A})A + \left(\frac{3}{2}c_4^2 + 8c_5c_9 - 30c_{10}^2A^2\bar{A}^2\right)A + \left((24c_7c_9 - 3c_4c_{10})A\bar{A} - 4c_4I\sigma\Omega\right)\bar{A}e^{i\sigma T_2} + (7c_4c_{10} + 8c_7c_9)A^3e^{-i\sigma T_2}\right]. \tag{B.5}$$

Appendix C. Some figures

In this appendix we report some zooms of figures reported in the text.

Data availability

No data was used for the research described in the article.

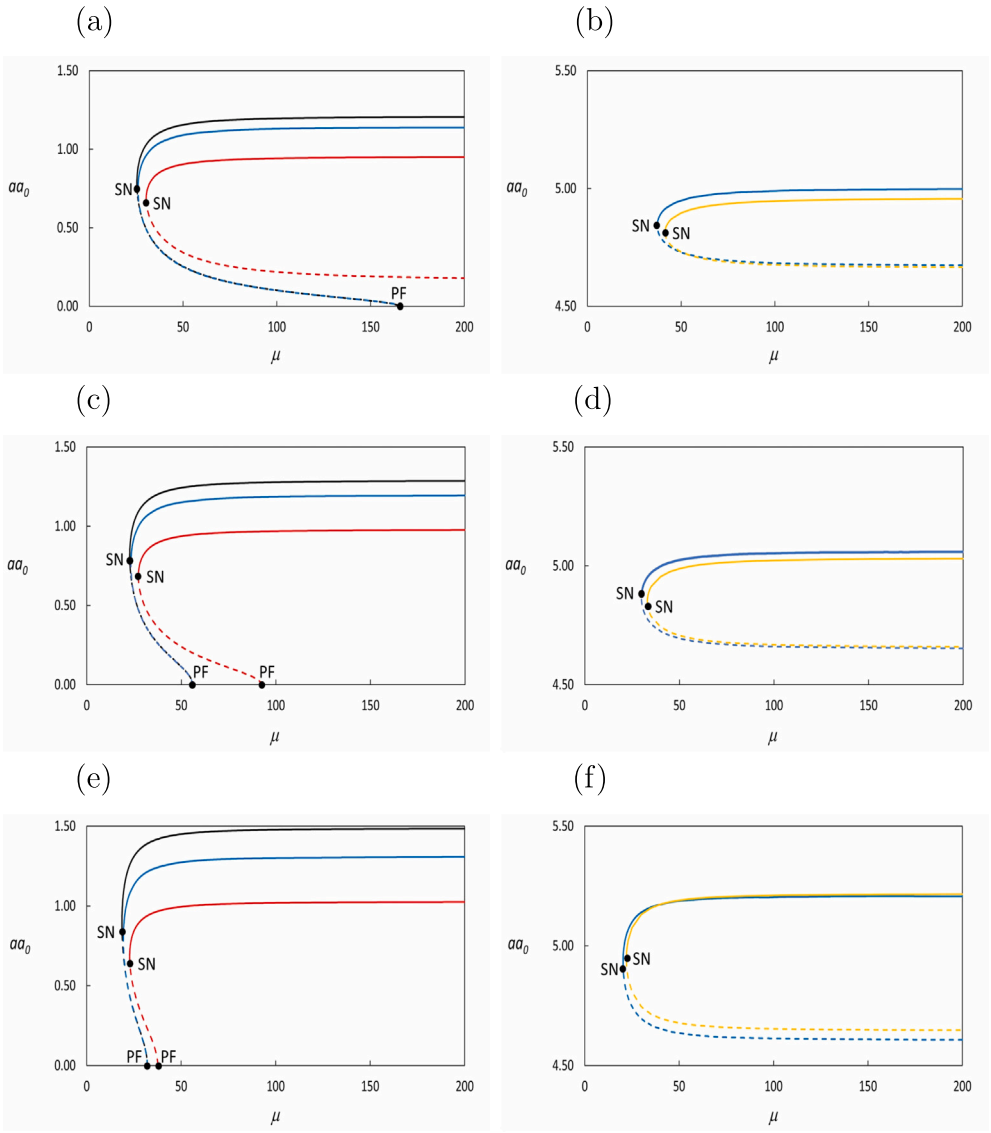

Fig. C.7. Zooms of Fig. 3(a), (c) and (e). The solutions $aa_0(\mu)$ for $\sigma\sigma/\Omega = 0.07$ (i.e. $\omega = 0.03699659115$ rad/s) and (a) and (b) $W = 0.9$ m; (c) and (d) $W = 1$ m; (e) and (f) $W = 1.2$ m. Black is the fifth order period-2 MTSM solutions, red the third order period-2 MTSM solutions, yellow the period-1 HBM solutions, blue the numerical solutions. Continuous lines are the stable paths, dashed lines the unstable paths. (a), (c) and (e) zooms for low values of aa_0; (b), (d) and (f) zooms for high values of aa_0.

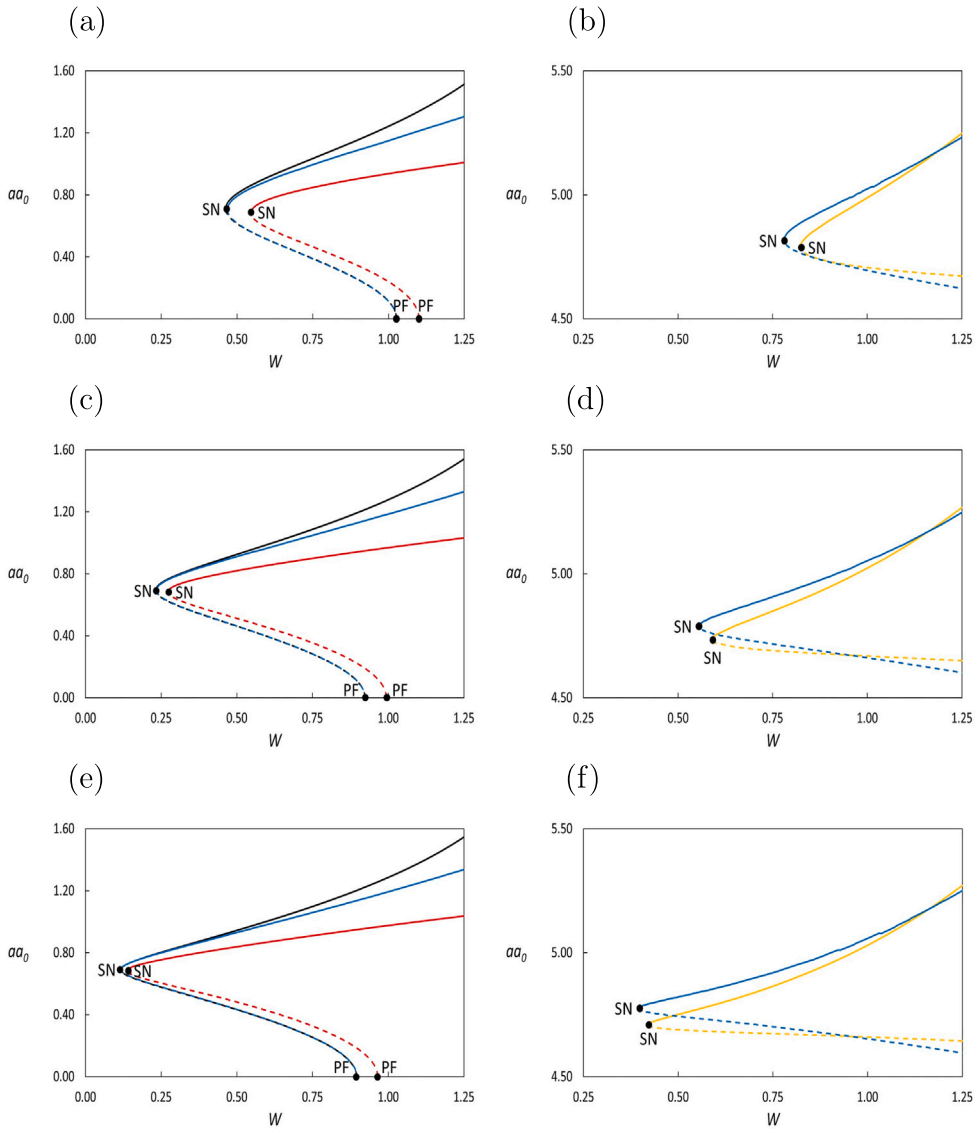

Fig. C.8. Zooms of Fig. 6(a), (c) and (e). The solutions $aa_0(W)$ for $\sigma\sigma/\Omega = 0.07$ (i.e. $\omega = 0.03699659115$ rad/s) and (a) and (b) $\xi = 0.02$; (c) and (d) $\xi = 0.01$; (e) and (f) $\xi = 0.005$. Black is the fifth order period-2 MTSM solutions, red the third order period-2 MTSM solutions, yellow the period-1 HBM solutions, blue the numerical solutions. Continuous lines are the stable paths, dashed lines the unstable paths. (a), (c) and (e) zooms for low values of aa_0; (b), (d) and (f) zooms for high values of aa_0.

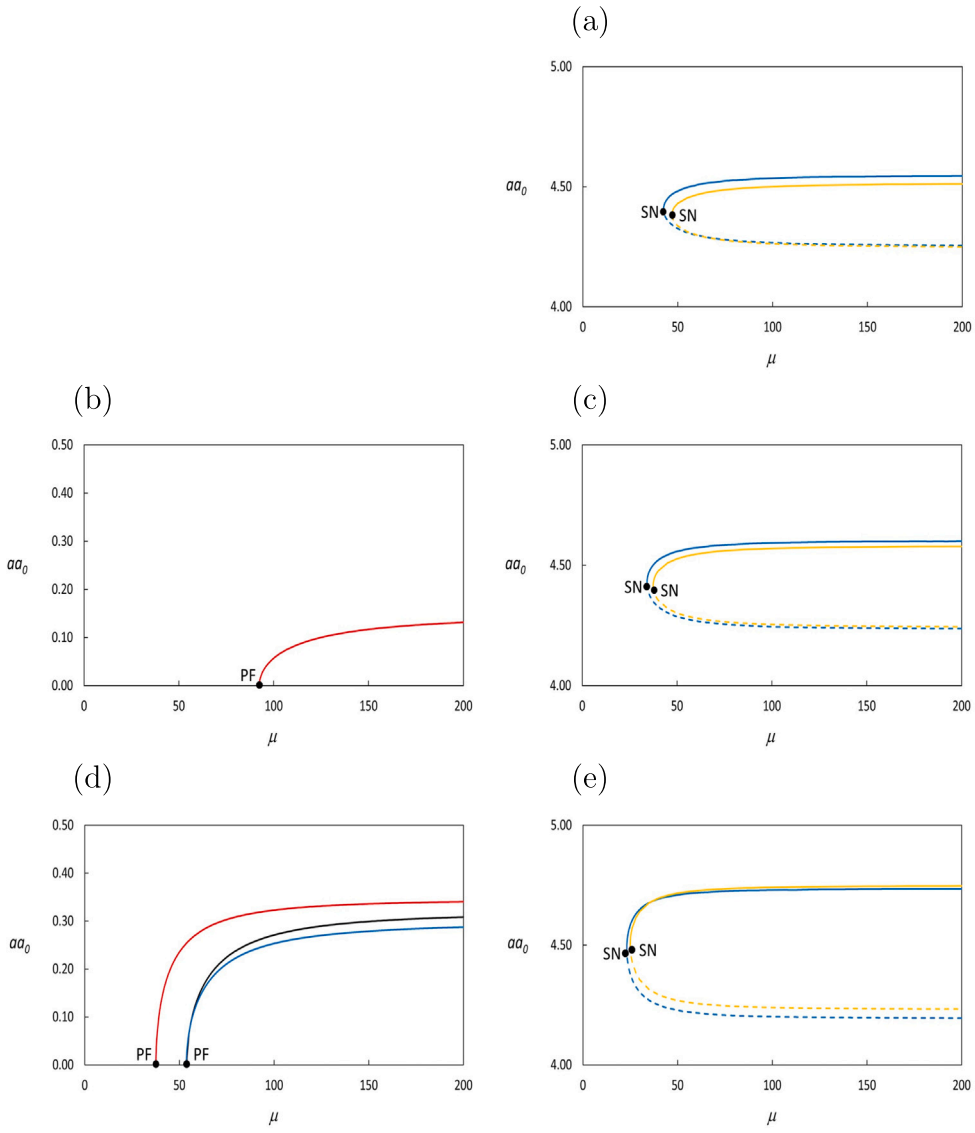

Fig. C.9. Zooms of Fig. 3(b), (d) and (f). The solutions $aa_0(\mu)$ for $\sigma\sigma/\Omega = -0.07$ (i.e. $\omega = 0.03449440625$ rad/s) and (a) $W = 0.9$ m; (b) and (c) $W = 1$ m; (d) and (e) $W = 1.2$ m. Black is the fifth order period-2 MTSM solutions, red the third order period-2 MTSM solutions, yellow the period-1 HBM solutions, blue the numerical solutions. Continuous lines are the stable paths, dashed lines the unstable paths. (b) and (d) zooms for low values of aa_0; (a), (c) and (e) zooms for high values of aa_0.

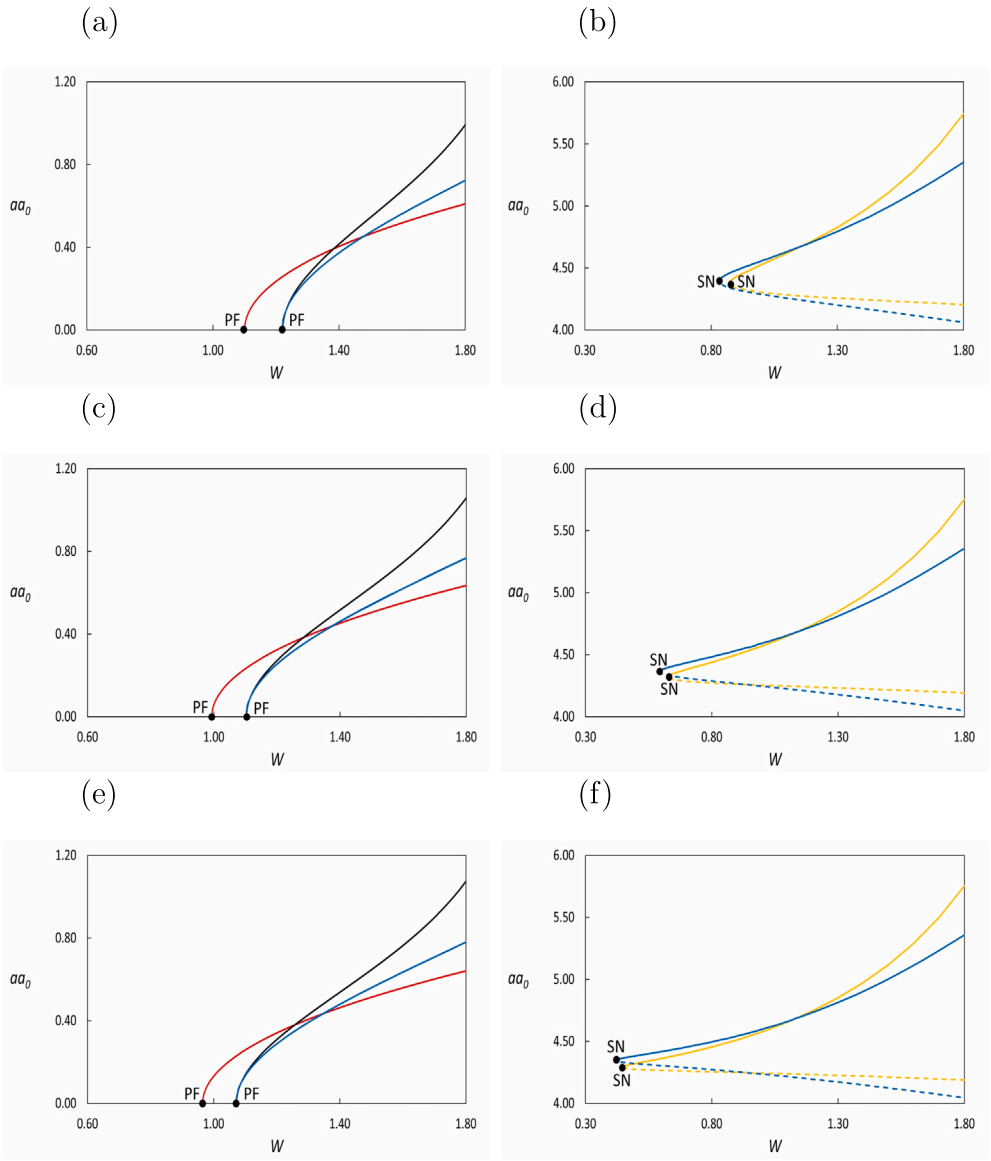

Fig. C.10. Zooms of Fig. 6(b), (d) and (f). The solutions $aa_0(W)$ for $\sigma\sigma/\Omega = -0.07$ (i.e. $\omega = 0.03449440625$ rad/s) and (a) and (b) $\xi = 0.02$; (c) and (d) $\xi = 0.01$; (e) and (f) $\xi = 0.005$. Black is the fifth order period-2 MTSM solutions, red the third order period-2 MTSM solutions, yellow the period-1 HBM solutions, blue the numerical solutions. Continuous lines are the stable paths, dashed lines the unstable paths. (a), (c) and (e) zooms for low values of aa_0; (b), (d) and (f) zooms for high values of aa_0.

References

[1] Agency IE. Key world energy statistics 2020. 2020, https://www.iea.org/reports/key-world-energy-statistics-2020. [Accessed July 2025].

[2] Sun X, Huang D, Wu G. The current state of offshore wind energy technology development. Energy 2012;41:298–312. http://dx.doi.org/10.1016/j.energy.2012.02.054.

[3] Benson CL, Magee CL. On improvement rates for renewable energy technologies: Solar PV, wind turbines, capacitors, and batteries. Energy 2014;68:745–51. http://dx.doi.org/10.1016/j.renene.2014.03.002.

[4] Ashuri T, Zaayer MB. Review of design concepts, methods and considerations of offshore wind turbines. In: Proceedings of the European offshore wind conference and exhibition. Berlin, Germany: European Wind Energy Association; 2007.

[5] Butterfield S, Musial W, Jonkman J, Sclavounos P. Engineering challenges for floating offshore wind turbines. Conference paper / technical report NREL/CP-500-38776, Golden, CO: National Renewable Energy Laboratory; 2007.

[6] Carbon Trust. Floating offshore wind: Market & technology review. Tech. rep., UK: Carbon Trust, Scottish Government; 2015.

[7] Marino E, Gkantou M, Malekjafarian A, Bali S, Baniotopoulos C, van Beeck J, Borg RP, Bruschi N, Cardiff P, Chatzi E, Čudina I, Dinu F, Efthymiou E, Ferri G, Gervásio H, Heng J, Jiang Z, Lenci S, Lukačević I, Manuel L, Meyer A, Méndez-Morales M, Osmanović A, Pakrashi V, Pandit A, Rega G, Skejić D, Tesch L, Ungureanu V, Uzunović T, Verma AS. Offshore renewable energies: A review towards floating modular energy Islands—Monitoring, loads, modelling and control. Ocean Eng 2024;313:119251. http://dx.doi.org/10.1016/j.oceaneng.2024.119251.

[8] Marino E, Gkantou M, Malekjafarian A, Bali S, Baniotopoulos C, van Beeck J, Borg RP, Bruschi N, Cardiff P, Chatzi E, Čudina I, Dinu F, Efthymiou E, Ferri G, Gervásio H, Heng J, Jiang Z, Lenci S, Lukačević I, Manuel L, Meyer A, Méndez-Morales M, Osmanović A, Pakrashi V, Pandit A, Rega G, Skejić D, Tesch L, Ungureanu V, Uzunović T, Verma AS. Offshore renewable energies: exploring floating modular energy islands—materials, construction technologies, and life cycle assessment. J Ocean Eng Mar Energy 2025. http://dx.doi.org/10.1007/s40722-025-00403-y.

[9] Jonkman JM, Matha D. Dynamics of offshore floating wind turbines - analysis of three concepts. Wind Energy 2011;14(4):557–69. http://dx.doi.org/10.1002/we.442.

[10] Ramachandran R, Desmond C, Judge F, Serraris J. Floating wind turbines: marine operations challenges and opportunities. Wind Energy Sci 2022;7(2):903–24. http://dx.doi.org/10.5194/wes-7-903-2022.

[11] Myhr A, Bjerkseter C, Ågotnes A, Nygaard TA. Levelised cost of energy for offshore floating wind turbines in a life cycle perspective. Renew Energy 2014;66:714–28. http://dx.doi.org/10.1016/j.renene.2014.01.017.

[12] Bak C, Bitsche RD, Yde A, Kim T, et al. Light rotor: The 10–MW reference wind turbine. In: Proceedings of EWEA 2012. European Wind Energy Association; 2012.
[13] Silva L, Cazzolato B, Sergiienko N, Ding B. Nonlinear dynamics of a floating offshore wind turbine platform via statistical quadratization - mooring, wave and current interaction. Ocean Eng 2021;236(12). http://dx.doi.org/10.1016/j.oceaneng.2021.109471.
[14] Davidson J, Henriques JC, Galeazzi R, Kalmár-Nagy T. Parametric resonance in wave energy converters and offshore wind turbines: A review. Renew Sustain Energy Rev 2025;220:115850. http://dx.doi.org/10.1016/j.rser.2025.115850.
[15] Mathieu E. Mémoire sur le mouvement vibratoire d'une membrane de forme elliptique. J Math Pures Appl 1868;13:137–203, Available at: https://www.numdam.org/item/JMPA_1868_2_13_137_0.pdf.
[16] Tondl A, Ruijgrok T, Verhulst F, Nabergoj R. Autoparametric resonance in mechanical systems. Cambridge University Press; 2000.
[17] Butikov EI. Simulations of oscillatory systems: with award-winning software, physics of oscillations. CRC Press; 2015.
[18] Rand R, Barcilon A, Morrison T. Parametric resonance of Hopf bifurcation. Nonlinear Dynam 2005;39:411–21. http://dx.doi.org/10.1007/s11071-005-3400-0.
[19] Champneys A. Dynamics of parametric excitation. In: Meyers RA, editor. Encyclopedia of complexity and systems science. New York, NY: Springer; 2009, p. 1–31. http://dx.doi.org/10.1007/978-3-642-27737-5_144-3.
[20] Bayat S, Allison JT. Impact of control strategies on the control co-design of spar floating offshore wind turbines. Ocean Eng 2025;336:121763. http://dx.doi.org/10.1016/j.oceaneng.2025.121763.
[21] Ma C, Iijima K, Nihei Y, Fujikubo M. Theoretical, experimental and numerical investigations into nonlinear motion of a tethered-buoy system. J Mar Sci Technol 2016;21(3):396–415. http://dx.doi.org/10.1007/s00773-015-0362-x.
[22] Choi EY, Jeong WB, Cho JR. Combination resonances in forced vibration of spar-type floating substructure with nonlinear coupled system in heave and pitch motion. Int J Nav Archit Ocean Eng 2016;8(3):252–61. http://dx.doi.org/10.1016/j.ijnaoe.2016.03.004.
[23] Choi E-Y, Cho J, Jeong W-B. Numerical study on the resonance response of spar-type floating platform in 2-D surface wave. Struct Eng Mech 2017;63:37–46. http://dx.doi.org/10.12989/sem.2017.63.1.037.
[24] Giorgi G, Davidson J, Habib G, Bracco G, Mattiazzo G, Kalmár-Nagy T. Nonlinear dynamic and kinematic model of a spar-buoy: Parametric resonance and Yaw numerical instability. J Mar Sci Eng 2020;8(7). http://dx.doi.org/10.3390/jmse8070504.
[25] Jingrui Z, Yougang T, Wenjun S. A study on the combination resonance response of a classic spar platform. J Vibr Control 2010;16(14):2083–107. http://dx.doi.org/10.1177/1077546309349393.
[26] Sang S, Zhou Y, Jiang XL. Study on nonlinear motion behavior of coupled heave-pitch for the classic spar platform based on AQWA. Appl Mech Mater 2012;170–173:2170–4. http://dx.doi.org/10.4028/www.scientific.net/AMM.170-173.2170.
[27] Gavassoni E, Gonçalves PB, Roehl DM. Nonlinear vibration modes and instability of a conceptual model of a spar platform. Nonlinear Dynam 2014;76:809–26. http://dx.doi.org/10.1007/s11071-013-1171-6.
[28] Rho JB, Choi HS, Shin HS, Park IK. A study on Mathieu-type instability of conventional spar platform in regular waves. Int J Offshore Polar Eng 2005;15(02). URL https://onepetro.org/IJOPE/article-pdf/2182426/isope-05-15-2-104.pdf.
[29] Shen W, Tang Y. Stochastic analysis of nonlinear coupled heave-pitch motion for the truss spar platform. J Mar Sci Appl 2011;10:471–7. http://dx.doi.org/10.1007/s11804-011-1093-y.
[30] Koo B, Kim M, Randall R. Mathieu instability of a spar platform with mooring and risers. Ocean Eng 2004;31(17):2175–208. http://dx.doi.org/10.1016/j.oceaneng.2004.04.005.
[31] Jang H, Kim M. Mathieu instability of arctic spar by nonlinear time-domain simulations. Ocean Eng 2019;176:31–45. http://dx.doi.org/10.1016/j.oceaneng.2019.02.029.
[32] Li Y, Liu L, Zhu Q, Guo Y, Hu Z, Tang Y. Influence of vortex-induced loads on the motion of spar-type wind turbine: A coupled aero-hydro-vortex-mooring investigation. J Offshore Mech Arct Eng 2018;140(5):051903. http://dx.doi.org/10.1115/1.4040048.
[33] Aziminia M, Abazari A, Behzad M, Hayatdavoodi M. Stability analysis of parametric resonance in spar-buoy based on floquet theory. Ocean Eng 2022;266:113090. http://dx.doi.org/10.1016/j.oceaneng.2022.113090.
[34] Ghozlane M, Najar F. Nonlinear analysis of a floating offshore wind turbine with internal resonances. Nonlinear Dynam 2024;112:1729–57. http://dx.doi.org/10.1007/s11071-023-09120-3.
[35] Zhao J, Liu Z, Lin X. Numerical study on 2:1 nonlinear parametric resonant responses of a spar buoy in waves. Appl Ocean Res 2025;154:104345. http://dx.doi.org/10.1016/j.apor.2024.104345.
[36] Zeng X, Shao Y, Feng X, Xu K, Jin R, Li H. Nonlinear hydrodynamics of floating offshore wind turbines: A review. Renew Sustain Energy Rev 2024;191:114092. http://dx.doi.org/10.1016/j.rser.2023.114092.
[37] Haider R, Li X, Shi W, Lin Z, Xiao Q, Zhao H. Review of computational fluid dynamics in the design of floating offshore wind turbines. Energies 2024;17(17). http://dx.doi.org/10.3390/en17174269.
[38] Li X, Xiao Q, Wang E, Peyrard C, Gonçalves RT. The dynamic response of floating offshore wind turbine platform in wave–current condition. Phys Fluids 2023;35(8):087113. http://dx.doi.org/10.1063/5.0158917.
[39] Haider R, Shi W, Lin Z, Xiao Q, Zhang W, Li X. Dynamic response of floating offshore wind turbine to focused wave excitation. Phys Fluids 2025;37. http://dx.doi.org/10.1063/5.0279082.
[40] Stewart G, Lackner M. Offshore wind turbine load reduction employing optimal passive tuned mass damping systems. IEEE Trans Control Syst Technol 2013;21(4):1090–104. http://dx.doi.org/10.1109/TCST.2013.2260825.
[41] Lara Ortiz M, Vazquez F, Sandua-Fernández I, Garrido J. Adaptive active generator torque controller design using multi-objective optimization for tower lateral load reduction in monopile offshore wind turbines. IEEE Access 2023;11:115894–910. http://dx.doi.org/10.1109/ACCESS.2023.3325840.
[42] Jonkman JM. Influence of control on the pitch damping of a floating wind turbine. In: Proceedings of the 2008 ASME wind energy symposium. no. NREL/CP-500-42589, Reno, Nevada: National Renewable Energy Laboratory; 2008.
[43] Davidson J, Henriques JC, Gomes RP, Galeazzi R. Opening the air-chamber of an oscillating water column spar buoy wave energy converter to avoid parametric resonance. IET Renew Power Gener 2021;15(14):3109–25. http://dx.doi.org/10.1049/rpg2.12204.
[44] Abe K, Utsunomiya T. Study on parametric excitation of a spar platform. J Struct Constr Eng 2012;68(2):813–22. http://dx.doi.org/10.2208/jscejam.68.I_813.
[45] Lamei A, Hayatdavoodi M, Riggs H, Ertekin R. Wave–current–wind interaction with elastic floating offshore wind turbines. Eng Anal Bound Elem 2025;171. http://dx.doi.org/10.1016/j.enganabound.2024.106052.
[46] Rho J-B, Choi H-S. Effect of a damping plate on Mathieu-type instability of a spar platform. J Soc Nav Archit Korea 2005;42(2):124–8. http://dx.doi.org/10.3744/SNAK.2005.42.2.124.
[47] Lenci S. Along-wind and cross-wind coupled nonlinear oscillations of wind turbine towers close to 1:1 internal resonance. Renew Sustain Energy Rev 2023;187:113698. http://dx.doi.org/10.1016/j.rser.2023.113698.
[48] Cameli A, Luciani M, Lenci S, Abdelak M, Ghiasi R, Malekjafarian A. Impact of soil-structure interaction on nonlinear modal coupling in 5MW monopile-supported offshore wind turbines under environmental conditions. IOP Conf Ser: Earth Environ Sci 2025;1552(1):012006. http://dx.doi.org/10.1088/1755-1315/1552/1/012006.
[49] Edwards EC, Holcombe A, Brown S, Ransley E, Hann M, Greaves D. Evolution of floating offshore wind platforms: A review of at-sea devices. Renew Sustain Energy Rev 2023. http://dx.doi.org/10.1016/j.rser.2023.113416.
[50] Gurley K, Kareem A. Simulation of ringing in offshore systems under viscous loads. J Eng Mech 1998;124(5). http://dx.doi.org/10.1061/(ASCE)0733-9399(1998)124:5(582).
[51] Wan L, Greco M, Lugni C, Gao Z, Moan T. A combined wind and wave energy-converter concept in survival mode: Numerical and experimental study in regular waves with a focus on water entry and exit. Appl Ocean Res 2017;63:200–16. http://dx.doi.org/10.1016/j.apor.2017.01.013.
[52] Jonkman J, Butterfield S, Musial W, Scott G. Definition of a 5-MW reference wind turbine for offshore system development. Technical report NREL/TP-500-38060, National Renewable Energy Laboratory; 2009.
[53] Qu X, Li Y, Tang Y, Hu Z, Zhang P, Yin T. Dynamic response of spar-type floating offshore wind turbine in freak wave considering the wave-current interaction effect. Appl Ocean Res 2020;100. http://dx.doi.org/10.1016/j.apor.2020.102178.
[54] Nayfeh A, Mook D. Nonlinear oscillations. Wiley classics library, Blacksburg: Wiley; 1979.
[55] Yan Z, Dai H, Wang Q, Atluri SN. Harmonic balance methods: A review and recent developments. CMES - Comput Model Eng Sci 2023;137(2):1419–59. http://dx.doi.org/10.32604/cmes.2023.028198.
[56] Krack M, Gross J. Harmonic balance for nonlinear vibration problems. 2019, http://dx.doi.org/10.1007/978-3-030-14023-6.
[57] Dai H, Yan Z, Wang X, Yue X, Atluri SN. Collocation-based harmonic balance framework for highly accurate periodic solution of nonlinear dynamical system. Internat J Numer Methods Engrg 2023;124(2):458–81. http://dx.doi.org/10.1002/nme.7128, arXiv:2203.02990.
[58] Chen Y, Hou L, Lin R, Song J, Ng T, Chen Y. A harmonic balance method combined with dimension reduction and FFT for nonlinear dynamic simulation. Mech Syst Signal Process 2024. http://dx.doi.org/10.1016/j.ymssp.2024.111758.
[59] Chen Y, Hou L, Lin R, Toh W, Ng T, Chen Y. A general and efficient harmonic balance method for nonlinear dynamic simulation. Int J Mech Sci 2024;276:109388. http://dx.doi.org/10.1016/j.ijmecsci.2024.109388.
[60] Chen Y, Jin Y, Lin R, Jiang Y, Mei X, Hou L, Wang Y, Yong NT, Guo A. Harmonic balance-automatic differentiation method: A practical nonlinear dynamics solver. Int J Mech Sci 2026;312:111192. http://dx.doi.org/10.1016/j.ijmecsci.2026.111192.
[61] Pizzolante F, Battarra M, Mucchi E, Cochelin B. Combining the asymptotic numerical method with the harmonic balance method to capture the nonlinear dynamics of spur gears. Mech Syst Signal Process 2024;214:111384. http://dx.doi.org/10.1016/j.ymssp.2024.111384.
[62] Wang Q, Yan Z, Dai H. An efficient multiple harmonic balance method for computing quasi-periodic responses of nonlinear systems. J Sound Vib 2023;554:117700. http://dx.doi.org/10.1016/j.jsv.2023.117700.

[63] Lin R, Hou L, Chen Y, Yuhong J, Saeed N, Chen Y. A novel adaptive harmonic balance method with an asymptotic harmonic selection. Appl Math Mech 2023;44:1887–910. http://dx.doi.org/10.1007/s10483-023-3047-6.

[64] Su O, Li Y, Li G, Cui Y, Li H, Wang B, Meng H, Li Y, Liang J. Nonlinear harmonic resonant behaviors and bifurcation in a two degree-of-freedom duffing oscillator coupled system of tension leg platform type floating offshore wind turbine. Chaos Solitons Fractals 2024;189:115656. http://dx.doi.org/10.1016/j.chaos.2024.115656.

[65] Zhang S, Tan G, Deng Y, Zhang Y, Wang Y, Wang Z. Vibration mitigation of spar-buoy floating wind turbines using a nonlinear energy sink. Ocean Eng 2024;304:117883. http://dx.doi.org/10.1016/j.oceaneng.2024.117883.

[66] Zhang SY, Lin Z, Li D, Deng Y, Zhang Y, Wang Y. Vibration suppression of spar-buoy floating wind turbines using a nonlinear stiffness combined inerter-based absorber. Ocean Eng 2025;329:121146. http://dx.doi.org/10.1016/j.oceaneng.2025.121146.

[67] Chen L, Basu B, Nielsen SR. Nonlinear periodic response analysis of mooring cables using harmonic balance method. J Sound Vib 2019;438:402–18. http://dx.doi.org/10.1016/j.jsv.2018.09.027.

[68] Chen L, Basu B, Nielsen S. Harmonic balance analysis of mooring cables. In: Conference: the 7th world conference on structural control and monitoring. 7WCSCM, Qingdao, China; 2018.

[69] Wang J, Dai W, Li T, Zhu X, Xu W, Xiong S. Optimization of nonlinear energy sinks for broadband vibration suppression in marine propulsion systems. J Vib Control 2026. http://dx.doi.org/10.1177/10775463251410791.

[70] Chizhevsky VN. Multistability in dynamical systems induced by weak periodic perturbations. Phys Rev E 2001;64:036223. http://dx.doi.org/10.1103/PhysRevE.64.036223.

[71] Habib G, Giorgi G, Davidson J. Coexisting attractors in floating body dynamics undergoing parametric resonance. Acta Mech 2022;233(6):2351–67. http://dx.doi.org/10.1007/s00707-022-03225-3.

[72] Settimi V, Lenci S, Rega G. Combined effect of wind and sea excitations on the internal resonance response of floating offshore wind turbines. Nonlinear Dynam 2025. http://dx.doi.org/10.1007/s11071-025-10905-x.